Solar Phys (2012) 277:89–118
DOI 10.1007/s11207-011-9821-7

SOLAR FLARE MAGNETIC FIELDS AND PLASMAS

Modeling and Interpreting the Effects of Spatial Resolution on Solar Magnetic Field Maps

K.D. Leka · G. Barnes

Received: 4 April 2011 / Accepted: 20 June 2011 / Published online: 27 July 2011
© Springer Science+Business Media B.V. 2011

Abstract Different methods for simulating the effects of spatial resolution on magnetic field maps are compared, including those commonly used for inter-instrument comparisons. The investigation first uses synthetic data, and the results are confirmed with *Hinode*/SpectroPolarimeter data. Four methods are examined, one which manipulates the Stokes spectra to simulate spatial-resolution degradation, and three "post-facto" methods where the magnetic field maps are manipulated directly. Throughout, statistical comparisons of the degraded maps with the originals serve to quantify the outcomes. Overall, we find that areas with inferred magnetic fill fractions close to unity may be insensitive to optical spatial resolution; areas of sub-unity fill fractions are very sensitive. Trends with worsening spatial resolution can include increased average field strength, lower total flux, and a field vector oriented closer to the line of sight. Further-derived quantities such as vertical current density show variations even in areas of high average magnetic fill fraction. In short, unresolved maps fail to represent the distribution of the underlying unresolved fields, and the "post-facto" methods generally do not reproduce the effects of a smaller telescope aperture. It is argued that selecting a method in order to reconcile disparate spatial resolution effects should depend on the goal, as one method may better preserve the field distribution, while another can reproduce spatial resolution degradation. The results presented should help direct future inter-instrument comparisons.

Keywords Active regions, magnetic fields · Active regions, models · Instrumental effects · Magnetic fields, photosphere · Polarization, optical

---

Solar Flare Magnetic Fields and Plasmas
Guest Editors: Y. Fan and G.H. Fisher

K.D. Leka (✉) · G. Barnes
CoRA Division, NorthWest Research Associates, 3380 Mitchell Ln., Boulder, CO 80301, USA
e-mail: leka@cora.nwra.com

G. Barnes
e-mail: graham@cora.nwra.com

1. Introduction

Understanding the limits of the data used to analyze and interpret the state of a system is a necessary part of remote-sensing science. For more than a century, the Zeeman effect in magnetically sensitive spectral lines has been used to detect and interpret the presence and character of solar magnetic fields. Much of solar physics research relies on interpreting magnetic field "maps" to investigate the physical state and dynamical evolution of the solar plasma. Quantities such as the magnetic field strength and direction, its variation (gradient) with space and time, the current density (or magnetic twist, current helicity, or shear angles, as preferred), plasma velocity vector inferred in part from the Doppler signal of the polarization spectra, and a variety of magnetic-related forces and torques are all of interest. They form the basis for our understanding of active region structure, large-scale field structure – even the dynamo(s), corona, and solar wind production. And they are all available from these measurements of the solar magnetic field, or are they?

With advancing capability of detector technology, modulator design and larger photon-gathering capabilities, it has become a challenge to reconcile the differing results from different instruments that engage different observing schemes, using different optical layouts and telescope sizes.

Comparison efforts between instruments and their resulting magnetic field maps are not new. Considerable effort has gone into comparisons between observing programs which produce the line-of-sight component over the whole solar disk (*e.g.*, Tran *et al.*, 2005; Demidov *et al.*, 2008; Demidov and Balthasar, 2009), as these data products provide input to heliospheric models which are the center of both ongoing research and real-time space-weather applications. Line selection and spectral sampling are crucial to consider for comparisons when the instruments and final data products may appear quite similar (Ulrich *et al.*, 2002, 2009). A challenging task is to compare instruments whose observing approaches are very different, as in the comparisons between the scanning-slit Advanced Stokes Polarimeter (ASP) and the filter-based SOUP instrument (Berger and Lites, 2002), the ASP and MDI (Berger and Lites, 2003), *Hinode*/SP and MDI (Moon *et al.*, 2007), and the ASP and the Imaging Vector Magnetograph (Labonte, Mickey, and Leka, 1999). The latter comparison attempted to evaluate the performance of two vector-field data sources, which means including the additional complications of the linear polarization and its data products (the component of the field perpendicular, or transverse to, the line of sight, and its azimuthal angle) in addition to the circular polarization and line-of-sight magnetic field component. Such an effort is not new (Wang *et al.*, 1992; Varsik, 1995; Bao *et al.*, 2000; Zhang *et al.*, 2003), and the effort required has not become simpler with time.

The spatial-resolution issue is the focus here. It has come to our attention, primarily through renewed efforts to inter-compare the performance of different facilities (the "Vector Magnetic Field Comparison Group", an ad hoc group of which the authors are members, that the manner in which different instrumental resolutions are incorporated into these comparisons can lead to erroneous results, in the direction of false confidence – implying that there is little or no impact to the resulting data due to spatial resolution, when we argue here that this is not the case.

Below we describe a way to model the gross effects from instrumental spatial resolution for spectro-polarimetric data, and demonstrate how this is required in order to avoid misleading results from *post facto* re-binning ("post-facto" here meaning "applied after the inversion from spectra to field", such that it is the magnetogram itself which is "rebinned"). We demonstrate, using both synthetic and real data, that spatial resolution differences do in fact lead to different results. On a positive note, in some cases the effects of varying spatial resolution behave in a predictable and systematic manner that depends on the structure of the observed solar feature, a result which can guide the interpretation of data obtained at any given spatial resolution.

2. Demonstration: Real Data

We begin with an example of the issue: we want to use data from two instruments interchangeably, so how do they compare? As an example, we take NOAA Active Region 10953 observed on 30 April 2007. For this date, there exist co-temporal data from both the Michelson Doppler Interferometer ("MDI") aboard the *Solar and Heliospheric Observatory* ("SoHO", Scherrer *et al.*, 1995), and from the Solar Optical Telescope/SpectroPolarimeter aboard the *Hinode* mission (Kosugi *et al.*, 2007; Tsuneta *et al.*, 2008); these exact data were used in De Rosa *et al.* (2009) as a boundary condition for nonlinear force-free extrapolations. The level-1.8.1 MDI "Full-Disk Magnetogram" from 22:24 UT 30 April 2007 samples with $1.98''$ at SoHO's L-1 location, which matches the optical spatial resolution of the telescope. The *Hinode*/SP scan which began at 22:30 UT 30 April 2007[1] is a "fast scan" which performs on-chip summation for the sub-critically sampled data, providing a final $0.3''$-sampled map that effectively matches the telescope resolution. The MDI and *Hinode*/SP maps are shown in Figure 1, where B_{los}, the line-of-sight component of the "pixel-area averaged" field is used for the *Hinode*/SP vector magnetogram to ensure a consistent comparison with the MDI map, where the fill fraction is assumed unity throughout. (For reference, a brief table of terminology used herein is included with Table 1.)

A sub-region of the MDI data is selected to match the *Hinode*/SP field of view, to within a fraction of an MDI pixel. The total of the unsigned data is computed (Table 2) at the original spatial sampling. We then "sampled" the *Hinode*/SP B_{los} map using the IDL "congrid" routine and recompute the total of the unsigned result. No further checks are made on the inter-instrument calibration. We explicitly do not quote uncertainties at this point: the uncertainties for the sums are significantly smaller than the differences between the compared data sets, and even the effect of a bias due to different photon noise levels is not significant in this case.

Why is there a difference between results from *Hinode*/SP and MDI? With studies showing that MDI generally underestimates the line-of-sight signal (Berger and Lites, 2003; Tran *et al.*, 2005; Ulrich *et al.*, 2009), it seems contradictory that the MDI result is the larger (see Appendix B). Some difference can be attributed to the different lines used and the different heights thus sampled (*e.g.*, Ulrich *et al.*, 2009), and the different inversion methods employed. Naively (or rhetorically) assuming that these differences are accounted for, the obvious remaining factor is the spatial resolution between the two datasets. Worse spatial resolution is expected to dilute a polarization signal (Leka, 1999; Orozco Suárez *et al.*, 2007); if this is the case, why is there only a tiny difference between the two "resolutions" of the *Hinode* data when rebinned in this manner?

3. Demonstration: Synthetic Data

Light entering a polarimeter is partially polarized, with the fraction and direction of polarization a function of many things including the strength and direction of the magnetic field along the photon ray-path above the photospheric $\tau = 1$ layer. Light entering a telescope

---

[1] Inversion from level-1D spectra to a magnetic map courtesy Dr. B.W. Lites, using the HAO Milne-Eddington inversion code (Skumanich and Lites, 1987) modified for *Hinode*/SP data, and presented to the authors for use in De Rosa *et al.* (2009).

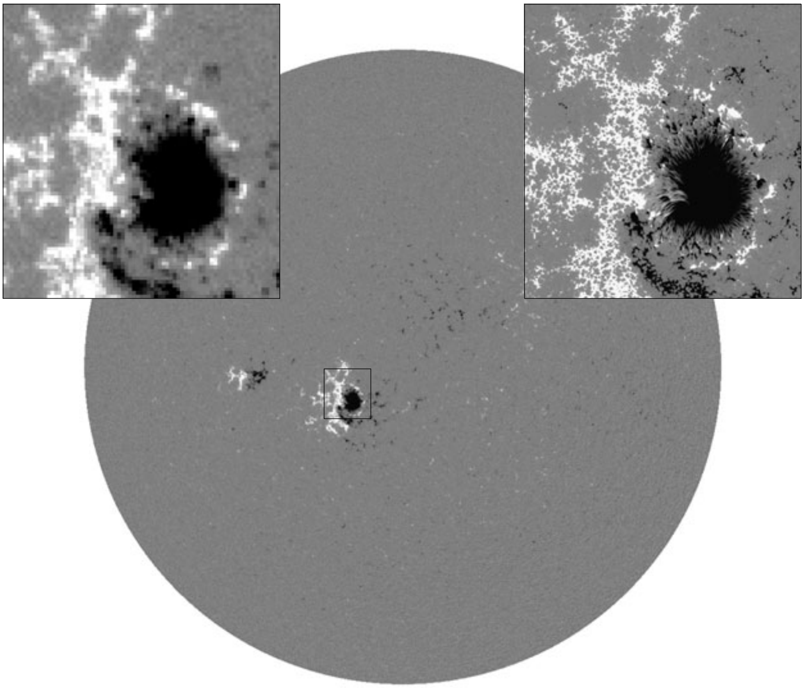

Figure 1 Data from the Michelson Doppler Imager (full-disk) line-of-sight component of the "pixel-area averaged" field B_{los} at 22:24 UT, 30 April 2007 includes NOAA Active Region 10953, delineated by a box. This area is also shown magnified (left inset). The same quantity for the same area on the Sun, derived from a Milne–Eddington inversion of *Hinode*/SpectroPolarimeter data obtained during 22:30 – 23:15 UT, 30 April 2007 is shown (right inset); all images are saturated at $\pm 500\ \text{Mx}\,\text{cm}^{-2}$ (Mx: maxwell).

Table 1 Table of Magnetic Field Terminology.

Term	Symbol (if appropriate)	Meaning
Field strength	B	Magnitude of the field (given in G (gauss))
Fill fraction	f	Fraction of a pixel filled with field
Inclination angle	γ	Inclination to the line of sight 0°, 180° along the line of sight, 90° in the plane of the sky
Azimuthal angle	ϕ	Azimuthal angle
"Pixel-area averaged"		Either $f = 1.0$ is assumed, or the inferred fill fraction has been multiplied through (given in $\text{Mx}\,\text{cm}^{-2}$).
Line-of-sight component	B_{los}	$fB \times \cos(\gamma)$
Transverse component	B_{trans}	$fB \times \sin(\gamma)$

includes mixed-polarization states, and optics to analyze the polarization generally follow the telescope entrance. The relevant quantities regarding the effects of spatial resolution for partially polarized light are d, the telescope diameter, and $I \pm P$, where P is any one (or a combination of) circular $[V]$ or linear $[Q,\ U]$ polarization signals, following the Stokes convention. The optical resolution varies (roughly) linearly with respect to d, meaning that the light which forms the respective Airy disk on a resolution element (a "pixel") is mixed

Table 2 Comparison of "Flux".

Data source	Pixel size (arcsec)	$\sum\|B_{\mathrm{los}}\|dA$ (10^{22} "Mx")	Difference from *Hinode*/SP original (%)
Hinode/SP	0.317	2.80	
Hinode/SP	1.98	2.84	1.2%
MDI	1.98	3.03	8.1%

to an extent determined by aperture size d prior to analysis optics (all other elements in the system being equal). Detected spectra are an intensity-weighted average which is a function of d, meaning that bright contributions will dominate.

3.1. Synthesis and Treatment of Synthetic Spectra

To investigate and demonstrate this effect, we turn first to synthetic data. The approach was briefly described in Leka *et al.* (2009b), and we present it in more detail here. Beginning with a synthetic magnetic model, the effects of different resolution (telescope size) on inferred magnetic field maps are obtained as follows:

- Generate emergent Stokes polarization spectra, $[I,\ Q,\ U,\ V]$ due to the Zeeman effect on a magnetically sensitive photospheric line, assuming a simple Milne-Eddington atmosphere.
- Combine the pure polarized spectra to produce "modulated" spectra $[I \pm P]$, *i.e.*, "observed" mixed-state light.
- Manipulate these spectra as desired, along the lines of:
  - add simulated photon noise by drawing from a Poisson distribution for each particular wavelength, with the expectation value set by the desired "noise level",
  - spatially bin (by summation) the modulated spectra to a desired spatial resolution,
  - average a temporal sequence of modulated spectra from a target location (from a temporal sequence of synthetic maps, as appropriate), and/or
  - apply an instrumental response function.
- Demodulate (combine in linear combination) the manipulated spectra back to pure Stokes $[I,\ Q,\ U,\ V]$.
- Re-invert using the inversion method of choice.

For these tests, spectra were computed using the analytic Unno–Rachkovsky equations applied for the magnetic field vector and velocity at each pixel, and thermodynamic/line parameters typical of the 630.25 nm Fe I spectral line ($g_{\mathrm{L}} = 2.5$, damping $a = 0.4$, Doppler width $\lambda_{\mathrm{D}} = 0.03$ Å, absorption coefficient $\eta_0 = 10$). Generating the Stokes spectra from the model field relied upon the spectra-genesis code which is part of the basic Milne-Eddington least-squares inversion routine "stokesfit.pro" (available from *SolarSoft* distribution[2]). This same inversion was then applied to the resulting Stokes spectra to produce a magnetogram, thus the assumptions underlying the genesis and the inversions for these test data are internally consistent; the goal here is not to test inversion methods *per se*. For the demonstrations here, the manipulation is limited to spatial binning.

3.2. The Magnetic Model

The synthetic magnetic model has a boundary field constructed specifically to include both areas of strong and spatially homogeneous field (reminiscent of sunspot umbrae) and areas

---

[2] http://www.lmsal.com/solarsoft/ssw_whatitis.html.

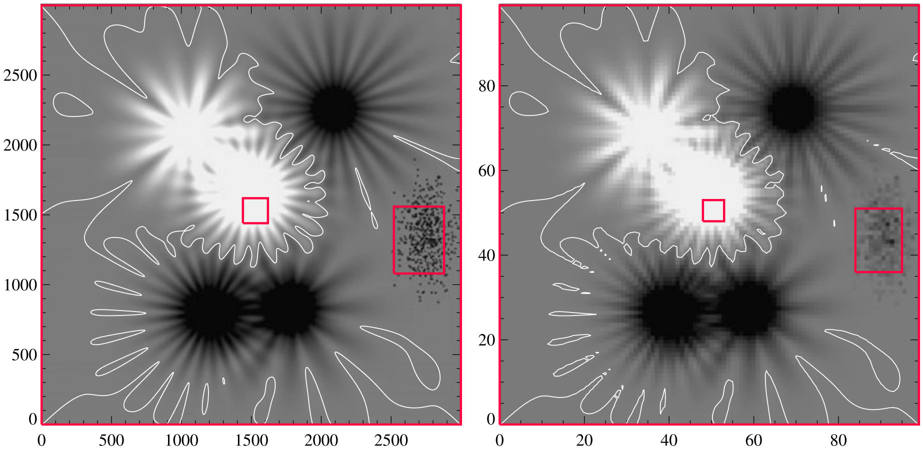

Figure 2 (Left) The "flowers" magnetic model B_z component (saturating at ±1000 G, $B_z > 0$ is white) at (left:) full resolution, 3000 × 3000 pixels arbitrarily set to have a 0.03″ size. Red boxes indicate the sub-regions highlighted in the later analysis, an "umbra" (180 × 180 pixels) and "plage" (360 × 480) areas. The smoothed polarity inversion line is shown as a white contour. (Right) Same, but after the spatial rebinning by a factor of 30 to a pixel size of 0.90″ (using the method of spatially binning the spectra,; see Section 3.1).

with significant fine-scale structure (with features resembling penumbral fibrils and plage area). Nicknamed the "Flowers" model (Figure 2), it is a potential-field construction that fully satisfies Maxwell's equations. It is (generally) resolved on the 3000 × 3000 computational grid, and a 0.03″ "pixel size" is assigned arbitrarily; this implies that the magnetic fill fraction is unity for each pixel. This synthetic boundary formed the basis of tests regarding the effects of spatial resolution on ambiguity-resolution algorithms for vector magnetic field data (Leka *et al.*, 2009b). We refer readers to that paper for a detailed description of its construction.

3.3. Signal Mixing in Spatially Averaged Stokes Spectra

The manipulations outlined above are the minimal steps necessary to model the effects of an observing system. Obviously we are completely ignoring the details of a full optical system or spatial smearing due to instrument jitter or atmospheric seeing effects. In addition, in this extremely limited demonstration we are completely ignoring any substantive difference between an imaging system and a slit-spectrograph polarimeter, and we are ignoring photon noise. Of additional note: there are no velocities in this synthetic model, which simplifies the spectral-mixing effects considerably: no asymmetries or additional broadening is introduced to the spectra. In short, the present study uses the simplest possible case.

We perform the spatial binning for a wide range of factors ranging from 2 to 60. We also include a unity bin factor, in order to have a consistent treatment of the spectra/inversion for comparison, rather than comparing to the raw synthetic model; in practice (as discussed in Leka *et al.*, 2009b) only a few pixels of the 9 million in the bin-1 case differ by more than machine precision from the original model field.

The effects of spatial resolution on the detected spectra are demonstrated in Figure 3. Consider two 10 × 10-pixel portions of the boundary, centered in the "umbra" and in the "plage", respectively. For each, samples from the 100 emergent demodulated Stokes spectra are shown. The emergent spectra for the umbral area are spatially very consistent (Figure 3

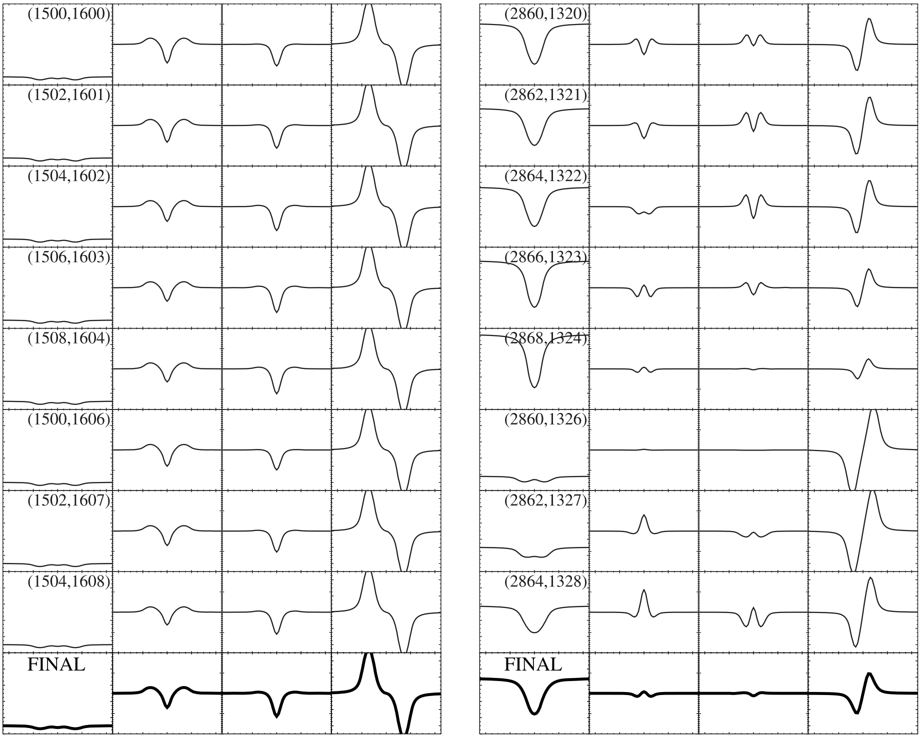

Figure 3 Left column: Eight samples of emergent Stokes $[I,\ Q,\ U,\ V]$ spectra, from a small patch (10×10 pixels) of the original synthetic (fully resolved) data, centered in an "umbra" at [1505, 1605] in Figure 2 (left). Stokes $[I,\ Q,\ U,\ V]$ are plotted left-right with ranges: $I : [0, 1]$, $Q,\ U : [-0.2, 0.2]$, $V : [-0.5, 0.5]$, the pixel coordinates (of the original model) are also shown. Left, bottom: The resulting "FINAL" $[I,\ Q,\ U,\ V]$ after averaging the 100 underlying emergent polarization spectra, plotted on the same scale. For this case, the resulting average is very similar to any of the sample contributing spectra. Right column: Same as left set, but for a 10×10 pixel area centered on the "plage" area, at [2865, 1325] in Figure 2 (left). In this case, the variability of the underlying spectra (top) leads to an average which differs noticeably from that arising from any single contributing pixel.

left), and the results of averaging the underlying 100 spectra are very similar to any individual contributing emergent spectra. On the contrary, the emergent spectra from the plage area (Figure 3 right) is spatially quite variable. There results a significant difference between the "spatially binned" resulting Stokes spectra and any single emergent spectrum from the underlying area.

Limited resolution causes an intensity-weighted averaging of the emergent Stokes polarization signals. It is often clear (from multiple lobes and extreme asymmetries, see Sanchez Almeida *et al.*, 1996; Sigwarth *et al.*, 1999; Grossmann-Doerth *et al.*, 2000) that the resulting observed spectra are inconsistent with a single magnetic field vector in a simple atmosphere having a linear source function and no additional gradients of any sort within the resolution element (the Milne–Eddington Unno–Rachkovsky assumptions). But sometimes it is not so clear (Sanchez Almeida, 1997). Since the underlying brightness distribution is unknown, untangling the weighting of the contributing spectra is impossible. This quick demonstration clearly cautions that while a strong signal cannot be created from nothing (instrumental

Table 3 Summary and Specifics of Binning Approaches.

Moniker	Algorithm	Code used	Details
"instrument"	Average modulated Stokes spectra	"awnoise.pro"[a] (modified)	"bin-5" implies averaging 5 × 5 spectra, then inverting
"Post-facto" approaches			
"average"	Simple average $B^i_{\mathrm{new}} = N_{\mathrm{bin}}^{-2} \sum_{j=1}^{N_{\mathrm{bin}}^2} B^i_j$	IDL "rebin" sample=0	Acts on image-plane field components[b] and field strength, fill fraction
"bicubic"	Bicubic Interpolation with $\boldsymbol{J} \times \boldsymbol{B} = 0$	"brebin.pro"[a]	Acts on ambiguity-resolved magnetograms
"sampled"	Simple sampling of image-plane field components[b] and field strength, fill fraction	IDL "congrid" center=1, interpolate=1	If bin is odd: use center point If bin is even: use average of central four points

[a] Available as part of http://www.cora.nwra.com/AMBIGUITY_WORKSHOP/2005/CODES/mgram.tar.

[b] Image-plane field components are defined as $B^i_{\mathrm{x}} = B_{\mathrm{trans}} \cos(\phi)$, $B^i_{\mathrm{y}} = B_{\mathrm{trans}} \sin(\phi)$, $B^i_{\mathrm{z}} = B_{\mathrm{los}}$, and are used to avoid wrap at $\phi = 0, 2\pi$.

and seeing effects aside, as well as any Doppler effects), a small or nonexistent signal can result even when there are strong underlying fields.

3.4. Creating Magnetograms

We now test the effects of the spatial binning of the polarization spectra on the ability of an inversion algorithm to retrieve the underlying structure. The synthetic binned spectra underwent an inversion using "stokesfit.pro"[3] which solves for the magnitude of the field in the instrument-frame B^i_{x}, B^i_{y}, B^i_{z}, and separately the magnetic fill fraction f (see Table 1). The resulting magnetograms were then ambiguity resolved using the minimum-energy code "ME0",[4] described in Leka *et al.* (2009b), Leka, Barnes, and Crouch (2009a). All parameters used for the inversion and ME0 were the same for each resolution (except those that scaled with array size), as it is not the intent to test either the inversion or the ambiguity-resolution algorithms *per se*. What results are vector magnetic field maps that simulate what would be observed through telescopes when solely the aperture size varies.

For comparison we perform three types of *"post facto"* binning on the bin-1 synthetic magnetogram, as summarized in Table 3. The three utilize a simple averaging (referred to as

---

[3] Implementation details: $[I,\ Q,\ U,\ V]$ default relative weighting: $1/[10, 2, 2, 1]$, fill fraction is fit, the initial guess set to the spatially binned parameters from the original model (*i.e.* as close to the solution as possible), "curvefit" specified unless a bad fit returned, in which case "amoeba" and "genetic" algorithms invoked for optimization.

[4] Available at http://www.cora.nwra.com/AMBIG/.

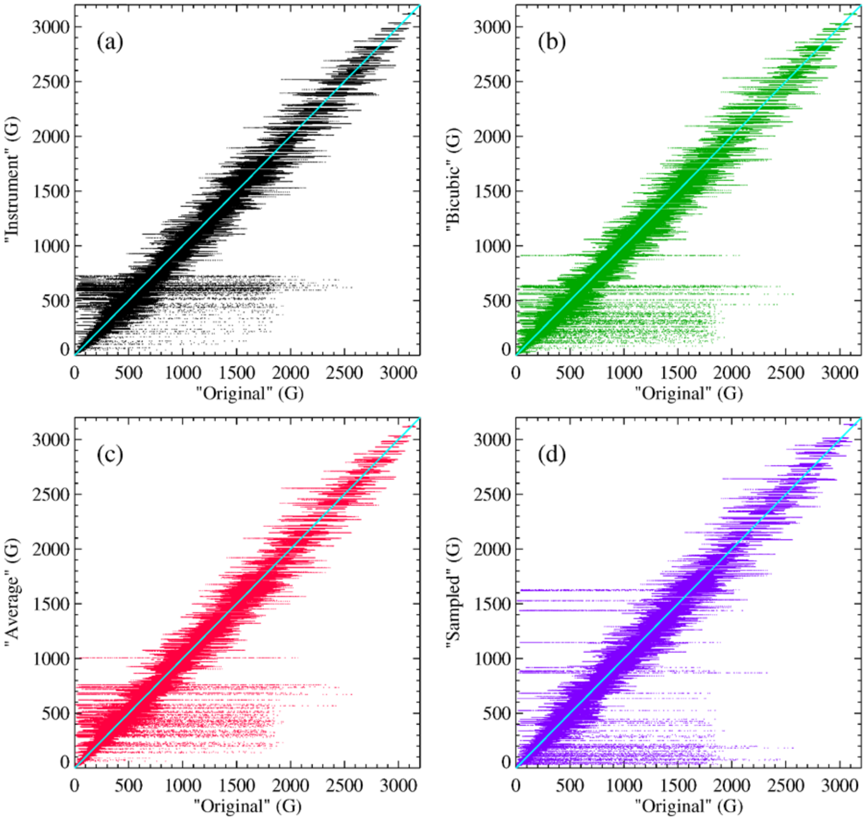

Figure 4 Intrinsic field strength B, comparing the original model magnetogram to the bin-by-30 results, for different binning approaches. (a) Original *vs.* **"instrument"**, (b) original *vs.* "bicubic", (c) original *vs.* "average", and (d) original *vs.* "sampled". For all, the $x = y$ line is also plotted for reference, and on the x-axis ("Original") are plotted all the values represented by the single resulting bin-30 pixel in question, whose value is plotted on the y-axis. Every other point in the binned magnetogram is shown, and every 3rd point of the 900 underlying values is plotted. The colors for these plots will be used consistently below.

"average"), a more sophisticated interpolation method developed by Dr. T. Metcalf specifically for the task of sampling vector magnetograms (**"interpolate"**), and a sampling approach which performs a minimal amount of averaging (**"sampled"**). We use color here and throughout for reference and clarity as the results of these methods are compared. For each of the "post facto" approaches, the azimuthal ambiguity resolution is an acute-angle method, matched to the results from ME0 for the "instrumental" approach at the same binning factor.

3.5. Comparing the Magnetograms

As seen in Figure 2, spatial rebinning of any sort produces a boxy, somewhat distorted magnetic field map. Quantitatively, however, which of the underlying field's properties are preserved and which are most affected by the change in resolution?

A scatter plot is a good starting place. In Figure 4 the intrinsic field strength B is compared between the original model and the four ways of binning. For all methods, the averaging produces a field that *generally* follows the underlying field distribution; this is reflected

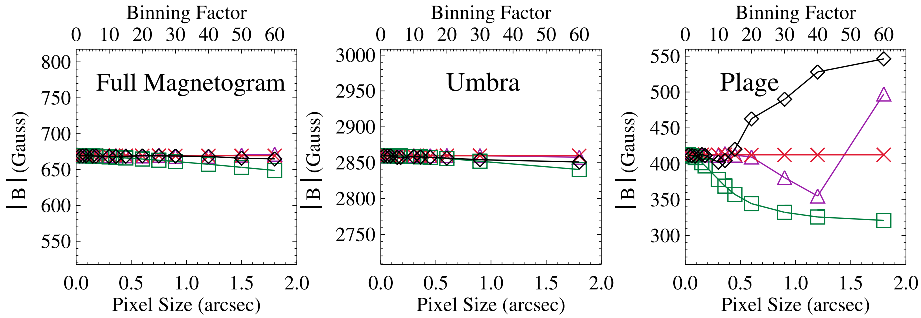

Figure 5 Average intrinsic field strength $\frac{1}{N}\sum B$ as a function of binning factor (top x-axis), for the four binning methods: **"instrument"** (◇), "bicubic" (□), "average" (×), and "sampled" (△). The three panels show, respectively, the full magnetogram, an "umbral" area and a "plage" area (see Figure 2). For each binning, N varies but the same sub-area of the "Sun" is covered; when non-integer pixel numbers result, that bin factor is omitted. The original model field is sampled at an arbitrarily set $0.03''$, the resulting "pixel sizes" are indicated (bottom x-axis). For these and all similar plots (except where noted), the y-axis ranges are kept consistent between the target areas for direct comparisons. Here, the effects are minimal for the full magnetogram and the "umbra", but have a much larger magnitude and differ between the binning methods in the "plage" area.

in that regression analysis returns a near-unity slope ($\gtrsim 0.98$) for each method. The extremes are lost in what may be termed the "weak-field" areas (up to ≈ 1 kG in the binned case) which are in fact highly structured.

Inversions can sometimes fail to return field strength separately from magnetic fill fraction, especially at low polarization signals. It has been shown that the product of these quantities is significantly more "robust", meaning easier to retrieve reliably (Bommier *et al.*, 2007) (but see also del Toro Iniesta, Orozco Suárez, and Bellot Rubio, 2010). Applying the same regression analysis to the product $f \times B$ indicates that this is not a cure for degraded spatial resolution: slopes and standard deviations which result differ almost imperceptibly, as do the underlying scatter plots, so we do not show them here.

We now examine the inferred magnetic components for the four binning methods ("instrument", "simple", "bicubic", and "sampled") for three target areas ("umbral", "plage", and the full field of view, see Figure 2), as a function of different binning levels. The nature of this comparison is shown in detail in Figure 5. The intrinsic field strength averaged over the (sub)-region in question, $\frac{1}{N}\sum B$ is shown as a function of binning factor for the three target areas. The results for the binning methods are shown for each sub-area. Comparisons following this format are presented for the magnetic fill fraction, the product of the fill fraction and field strength, and the inclination angle distribution (Figure 6). The total unsigned magnetic flux $\Phi = \sum f|B_z|dA$ (Figure 7) is presented, acknowledging the somewhat arbitrary assignment of pixel size. The inferred vertical electric current density $J_z = C\nabla \times fB_h$ was computed for the maps using a finite-difference method that employs a 4-point stencil (Canfield *et al.*, 1993) and C includes all the appropriate physical constants; from this, the total unsigned vertical current $I = \sum |J_z|dA$ is presented (Figure 7) with the same acknowledgement regarding the assigned pixel size as above.

The most significant difference between the plage and umbral areas in the synthetic data is the fact that the former comprises small-scale structure. The umbral area has essentially one magnetic center, whereas the plage area contains a few hundred centers that are highly localized with almost field-free regions separating each center. The different underlying

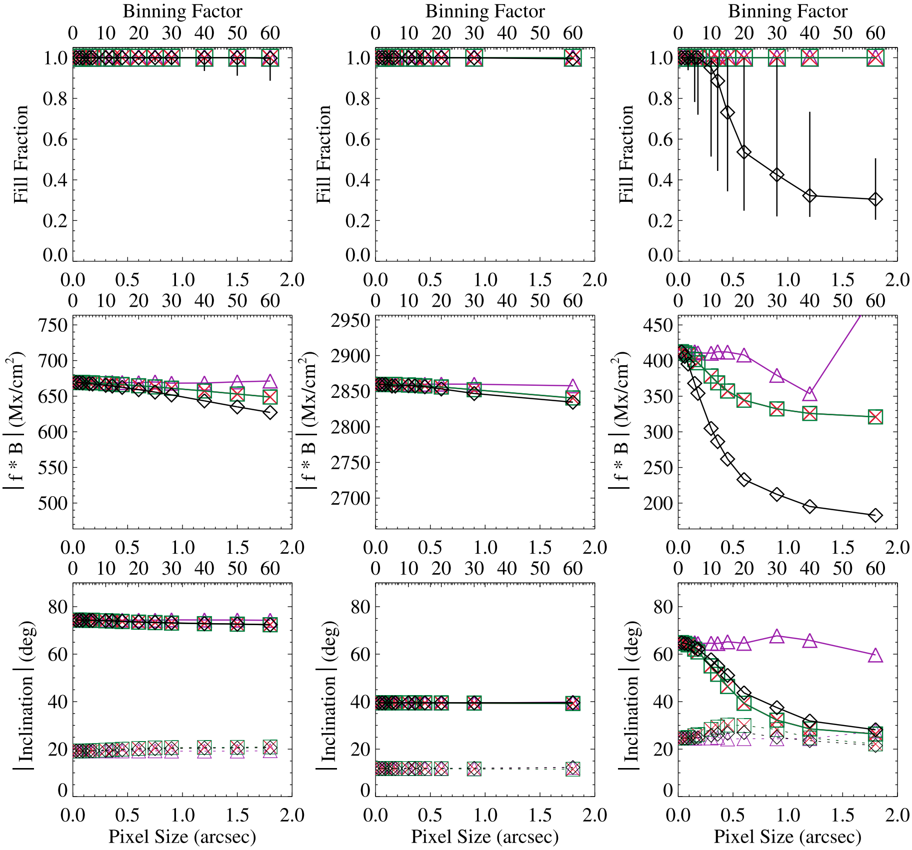

Figure 6 The same format as in Figure 5. Top row: Median (symbols) and 10th, 90th percentiles (displayed as "error bars") of inferred magnetic fill fraction as a function of bin factor. The three "post-facto" approaches consistently return unity since the original model (and bin-1 inversion) have unity fill fraction throughout. Middle row: The average product of the fill fraction and field strength, $\frac{1}{N}\sum fB$ as a function of binning factor. Bottom row: Variation of the average inclination angle with binning factor (thick line-connected curves), 0° indicates (unsigned) fields directed along the line of sight, or pure B_{los}, and 90° indicates field perpendicular to the line of sight or pure B_{trans} (here, $\gamma = \tan^{-1}(B_{\text{trans}}, |B_{\text{los}}|)$). Dot-connected curves indicate the standard deviation of the angle distribution.

structure of the field leads to different behavior at different "spatial resolutions", according to the approach.

For field strength (Figure 5), none of the methods show dramatic differences in the umbral area; the same is true for the "full magnetogram". In the plage area, the methods behave quite differently. Simple rebinning shows absolutely no change with bin factor, consistent with its approach of numerically averaging the positive-definite input. The bicubic approach shows a decrease in average field strength, as interpolation increasingly underestimates the strong field strength in the scattered magnetic centers. The sampling follows the simple averaging until approximately bin-20 when it decreases, before abruptly increasing at bin-60. When the bin factor is small, the sum over the subset of sampled points gives a reasonable approximation to the sum over all the (bin-1) points. As bin factor increases, the number of sampled points used to represent the sum decreases, and the result is likely to be increasingly large changes, but with no consistent trend toward increasing or decreasing with bin factor. The instrument binning in the plage area similarly shows minimal effect until approximately bin-10, beyond which the average field strength in the plage area increases. The polarization-free “gaps” between centers begin to be “contaminated” with polarization at higher bin factors, and the resulting average field strength increases, in part because this synthetic plage area is unipolar.

The inversion method separately fits for the field strength and the magnetic fill fraction (Table 1). The synthetic model is fully resolved, so that for bin-1 all pixels return unity fill fraction, and hence all “post-facto” approaches maintain unity fill fraction for all bin factors. When an inversion is performed on spatially averaged spectra, there is almost no effect in the umbral area (Figure 6, top): the median fill fraction remains unity. The situation is very different in the plage area: the non-unity median and wide *range* of fill fraction returned clearly indicate that worsening resolution leads to unresolved structures. The full field of view results reflect a mix of influences from the “resolved” and “unresolved” areas in the field of view.

Whether the underlying structures are resolved or not as indicated by non-unity fill fraction, clearly appears to factor into how worsening spatial resolution will affect the field distribution. The product of fill fraction and field strength (Figure 6) which is arguably a better measure of inversion output, is the same as the field strength for the “post-facto” approaches, but shows a dramatic drop under “instrument” binning. The increase in field strength is more than compensated by a decreasing fill factor, likely as a result of the intensity weighting of the average Stokes spectra.

Other effects of note: the distribution of inclination angle (Figure 6, bottom) with worsening spatial resolution is impacted so as to imply an average orientation closer to the line of sight in the plage than is originally present, for all but the “sample” approach. In other words, with worse spatial resolution the B_{los} begins to dominate over B_{trans}, which might be expected given the lower fractional polarization signal for linear as compared to the circular polarization.

The total magnetic flux (Figure 7) is almost insensitive to bin factor if one uses a post-facto approach, yet plummets with the instrument approach. The sampling approach is slightly variable, again since the value selected will almost randomly hit strong or weak signal as the bin factor increases. Still, the difference is clear: post-facto binning of any kind does not reproduce the effect of spatial resolution.

The total electric current (Figure 7) *increases* with bin factor overall, with a more pronounced effect in unresolved areas than in the unity-fill-fraction umbral region. Recalling that the underlying magnetic model is potential, this somewhat surprising initial increase and the subsequent decrease in plage areas is due to an interplay between the less-smooth map (see Figure 2), and the finite differences used to calculate the vertical current (see the discussion in Leka *et al.*, 2009b); also at play are the influence of the spatial resolution on the relative strength of the horizontal component (as seen through the variation in the inclination angle) and the magnetic fill fraction, which is included when calculating the vertical current density. The bicubic approach, which attempts to include the field structure in the approach, is least affected while the sampling produces the greatest spurious total current. Comparing the results for the umbra and plage sub-area to the full field of view, it is clear that most of the resulting current arises from unresolved areas such as the “penumbra-like” regions that dominate the synthetic model.

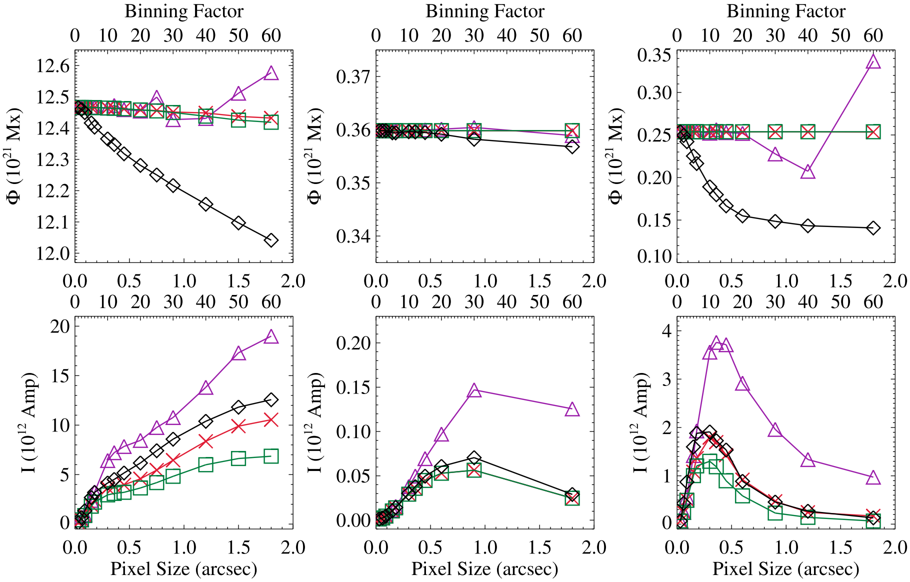

Figure 7 Variation with spatial resolution of parameters often used for characterizing active regions. Top: The total unsigned magnetic flux $\Phi = \sum f|B_{\mathrm{z}}|dA$. Bottom: The total unsigned electric current $I = \sum |J_{\mathrm{z}}|dA$. For these plots, the y-axis ranges vary.

3.5.1. Statistical Tests of Similarity

The question remains how best to characterize the differences in the results at different spatial resolutions. We see from the previous analysis that the resulting magnetograms do differ, but can they adequately describe the underlying field?

We perform Kolmogorov–Smirnoff tests on the distribution of the resulting field parameters to investigate how well a lower-resolution map characterizes the highest-resolution map. The K–S test uses the cumulative probability distribution (CPD) to compare two samples. Two parameters result: "P", the probability of rejecting the null hypothesis, and the "D"-statistic, which measures the maximum difference between the two CPDs. In this case the null hypothesis can be stated, "The two samples arise from the same population", the two samples being, *e.g.*, the map of $B(x, y)$ from the full-resolution data and the map from a binned-resolution magnetogram. It should be remembered that for a given K–S D-statistic, the KS-probability statistic is extremely sensitive to changes in the sample sizes, which is very much the case when the bin factor becomes large.

Comparisons of the CPDs for field strength and vertical current density (Figure 8) confirm that the widest differences imposed at the bin-30 level occur in the plage area. Other parameters (inclination angle, etc.) show similar behavior. The umbral area and the similarity between the CPDs there and the full magnetogram would lead us to believe (correctly, as demonstrated in Figure 6) that for this model, the full magnetogram area is dominated by areas of high fill fraction while still containing areas of unresolved highly structured field.

For the distribution of field strength, the D-statistic (Figure 9) is dominantly zero for the full field of view, and increases only slightly with worse spatial resolution in the umbra. However, it is significantly non-zero for the "plage" area, reflecting that all bin factors show the same behavior seen in detail in Figure 8. The smallest D-statistic in the plage area comes

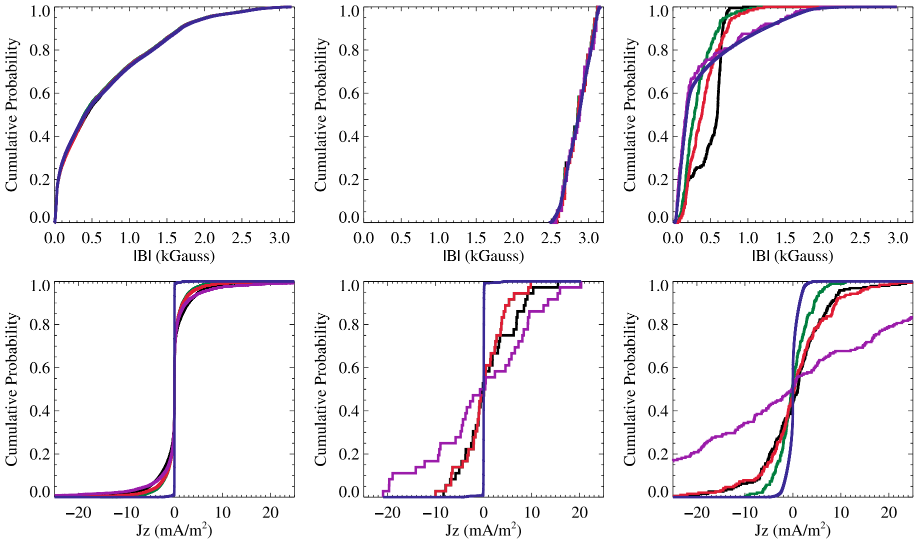

Figure 8 Cumulative probability distributions, comparing that for the full-resolution synthetic map to the bin-30 results, for the three fields of view (entirety, "umbra", and "plage" areas). For each, CPD curves are plotted for the original resolution, the **instrument** method, and the bicubic, average, sampled post-facto approaches. The top row is for the intrinsic field strength B, and the bottom row is for the vertical electric current density J_z.

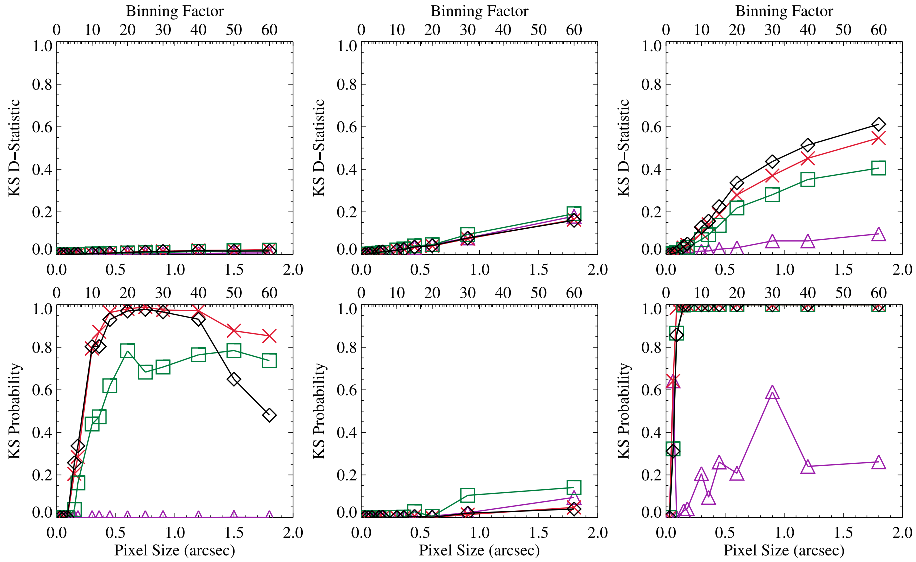

Figure 9 Again for the three fields of view, summaries of the Kolmogorov–Smirnoff tests as a function of binning factor, for the field strength B. The top row shows the D-statistic, and the bottom row shows the probability P that the two samples considered are *different* (see text). Shown are four curves, original resolution *vs.* "instrument" (◇), "bicubic" (□), "average" (×), and "sampled" (△) magnetograms.

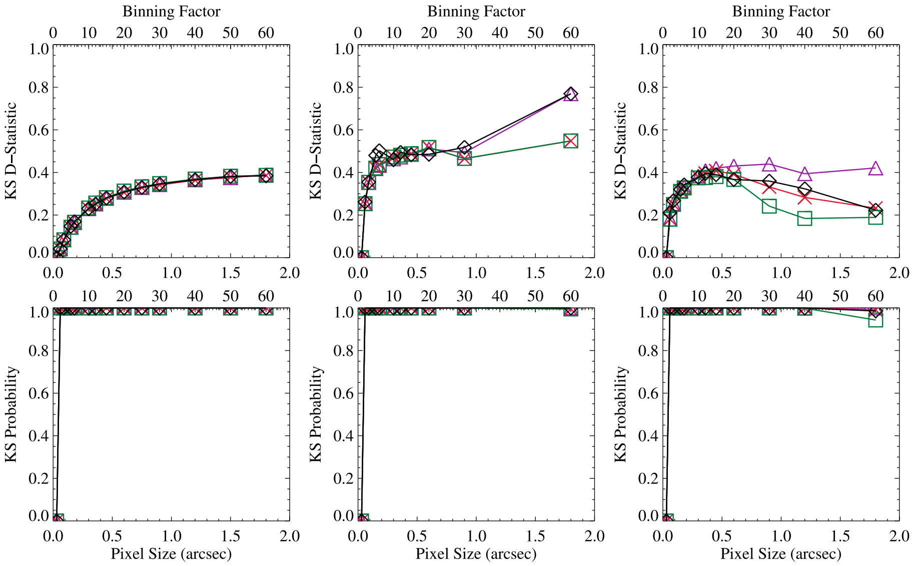

Figure 10 Summaries of the Kolmogorov–Smirnoff tests as a function of binning factor, for the vertical electric current density J_z. Format follows Figure 9.

from the sampling approach; the greatest from the instrumental approach. The probabilities of rejecting the null hypothesis are mixed but generally close to unity for the plage area, with systematically lowest probabilities for sampling, as expected.

For the distribution of J_z, a quantity derived by taking derivatives of the field distribution, the K–S D-statistic (Figure 10) is significantly non-zero for all three sub-areas and all methods at all spatial resolutions. The KS-probability is consistently unity; this bodes ill for the possibility that unresolved magnetograms recover the underlying distribution of field or vertical current.

To summarize these results, in areas such as this model "umbra", the underlying field varies little and the inferred fill fraction is consistent with it being "resolved". It can be argued that through a wide range of spatial resolution, the inferred field distribution represents the underlying field. The situation for highly structured underlying field is very different: areas of low and mixed fill fraction imply that the field is not resolved. It is fairly clear that instrumental effects on the spectra result in a substantively different field distribution, and the implied structures should be treated with much less confidence. And, with all caveats acknowledged due to the use of synthetic data, we find that in general, inferring the distribution of the vertical current is very susceptible to the effects of spatial resolution.

4. Demonstration: Real Data, Revisited

One may always argue that synthetic data constructed to demonstrate a particular effect may not represent observational "truth". Hence, we perform the same exercise using data from the Solar Optical Telescope SpectroPolarimeter aboard the *Hinode* mission (Tsuneta *et al.*, 2008). While the data from this instrument are arguably not the highest-resolution spectropolarimetric data available, the temporal and spatial consistency coupled with very good resolution in both spatial and spectral dimensions make these data ideal for this purpose.

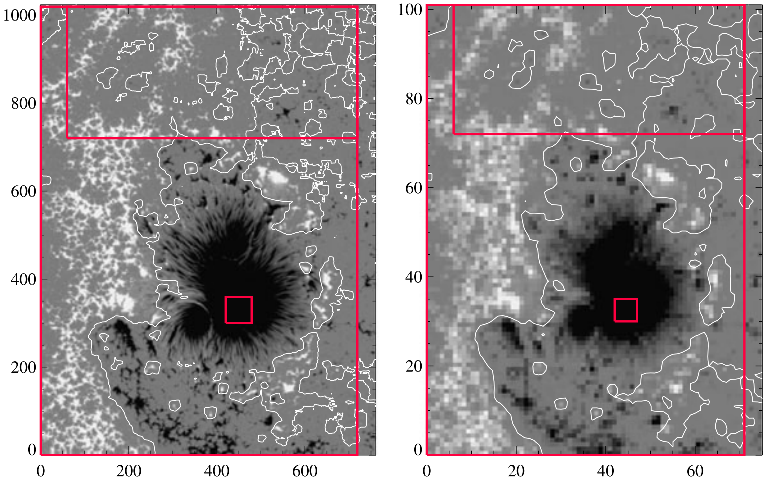

Figure 11 The B_{los} component inferred by *Hinode*/SP, scaled to ±1000 Mx cm^{-2}, for NOAA Active Region 10953 observed at 18:35 UT, 30 April 2007. Left: Full-resolution data, with original dimensions 762 × 1024 and 0.15″ pixels size. Boxes indicate the sub-regions highlighted in the later analysis, "umbra" (60 × 60 pixels), "plage" (660 × 300). In addition, as shown the "full field of view" is slightly trimmed (to 720 × 1020) to ensure integer divisibility by a range of factors. Right: Same, after "instrument" binning by a factor of 10, to 1.5″.

We chose the 18:35 UT scan of 30 April 2007 scan of NOAA Active Region (AR) 10953, observed at S09.5, E11.5 ($\mu = 0.98$), which was a "normal" scan that approximately matches scan-steps to the slit width and does not perform any on-board summation. The field of view includes a sunspot and plage area sufficient for this purpose. The pixels are not exactly square, and are not interpolated to be square, but treated as unequal in dimension for all of the analysis; we do, however, use the average of 0.15″ when referring to general pixel size.

An approach parallel to that described above was used to treat the *Hinode*/SP data, albeit beginning with the fully calibrated Level-1D $[I,\ Q,\ U,\ V]$ Stokes spectra.[5] In this case there is already photon noise present in the data, and the demodulation is performed on-board. In the context of the Poisson-statistics (see Appendix A), the implications are that we cannot exactly model the effects of different apertures. Without the "raw" observed modulated $I \pm P,\ P \in [Q,\ U,\ V]$ spectra and the different contributing realizations of noise, information has already been lost, and manipulating the demodulated pure $[I,\ Q,\ U,\ V]$ spectra is equivalent to reconstructed mixed-polarization states. The manipulated (averaged spatially by summation) spectra will present with lower noise than would actually be the case, but the primary effects of spatial resolution modeling will still be apparent.

The binned spectra were written in the "ASP" format (with a reformatter courtesy B. Lites, HAO/NCAR), and inverted using the HAO/NCAR Milne-Eddington inversion code "sss-inv" (Skumanich and Lites, 1987; Lites and Skumanich, 1990; Lites *et al.*, 1993, with minor modifications for *Hinode*/SP specifics, again courtesy B. Lites, HAO/NCAR).[6] The

---

[5] http://sot.lmsal.com/data/sot/level1d/.

[6] Implementation details: $[I,\ Q,\ U,\ V]$ weighting:$1/[100, 1, 1, 10]$, fill fraction solved, initial guess via "genetic" algorithm optimization, all pixels inverted (no minimum-polarization threshold), "scattered light" profile determined where $\sum |P| < 0.4\%$.

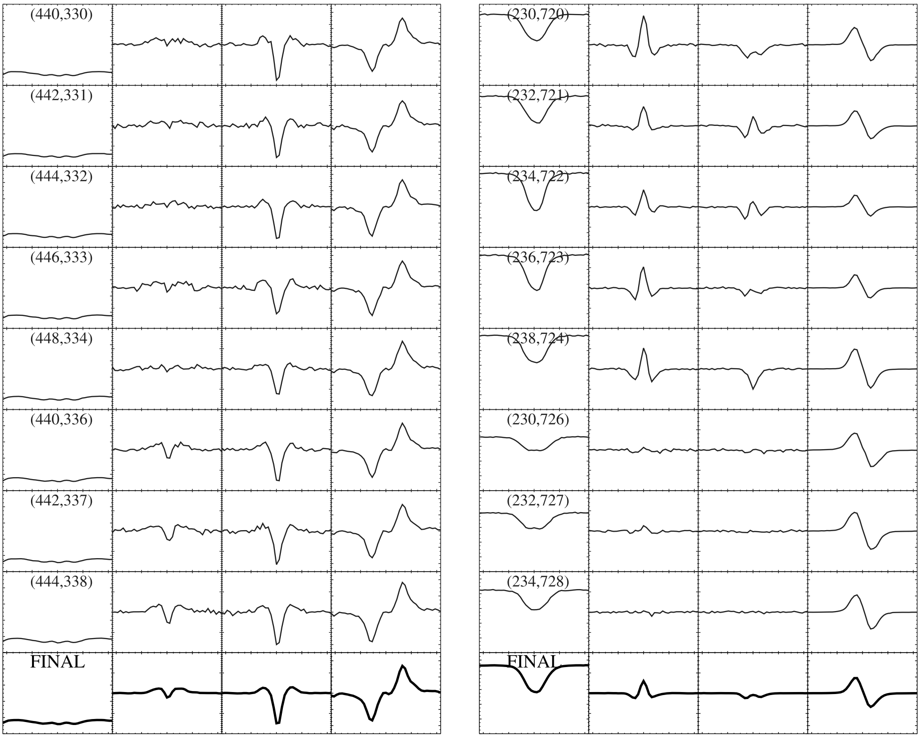

Figure 12 Left column: Eight samples of emergent Stokes $[I,\ Q,\ U,\ V]$ spectra, from a small patch (10×10 pixels) of the full-resolution *Hinode*/SP map, centered in the sunspot umbra at [445, 335] in Figure 11(left). Stokes $[I,\ Q,\ U,\ V]$ are plotted left-right with ranges: $I:[0,1],\ Q,\ U:[-0.2,0.2],\ V:[-0.5,0.5]$, the pixel coordinates (of the original data) are also shown. Left, bottom: The resulting "FINAL" $[I,\ Q,\ U,\ V]$ after averaging the 100 underlying emergent polarization spectra, plotted on the same scale. Right column: Same as left set, but for a 10×10 pixel area centered in the "plage" area, at [235, 725] in Figure 11 (left). For these plage data, the ranges are $I:[0,1],\ Q,\&\ U:[-0.1,0.1],\ V:[-0.5,0.5]$.

full-resolution data were subjected to the same reformatting and inversion (without binning) to ensure a consistent comparison. The "ME0" minimum-energy code was used in a consistent manner for ambiguity resolution for all data, and J_z was calculated in exactly the same manner as for the synthetic data. A sample binned magnetogram is shown in Figure 11.

As with the synthetic data, three areas are analyzed: the full field of view, and then separately two areas, one centered on the sunspot umbra and another on a plage area to the north of the sunspot (Figure 11). The latter area was chosen to avoid the emerging filament at the south east edge of the sunspot (Okamoto *et al.*, 2008). The full scan was trimmed slightly and both sub-areas were chosen to be evenly divisible for a number of binning factors.

Samples of the effects of "instrument" binning on emergent Stokes spectra from the *Hinode*/SP data are shown in Figure 12. The umbral sample displays very consistent Stokes spectra, and a final bin-10 result that closely resembles any single constituent-pixel's set of spectra. The noise is nicely reduced in the binned spectra (although somewhat artificially, as described above and in Appendix A). The plage sample demonstrates exactly the effect shown in Figure 3, that the constituent spectra are quite variable, and the resulting binned data reflect an average that does not represent any single underlying pixel.

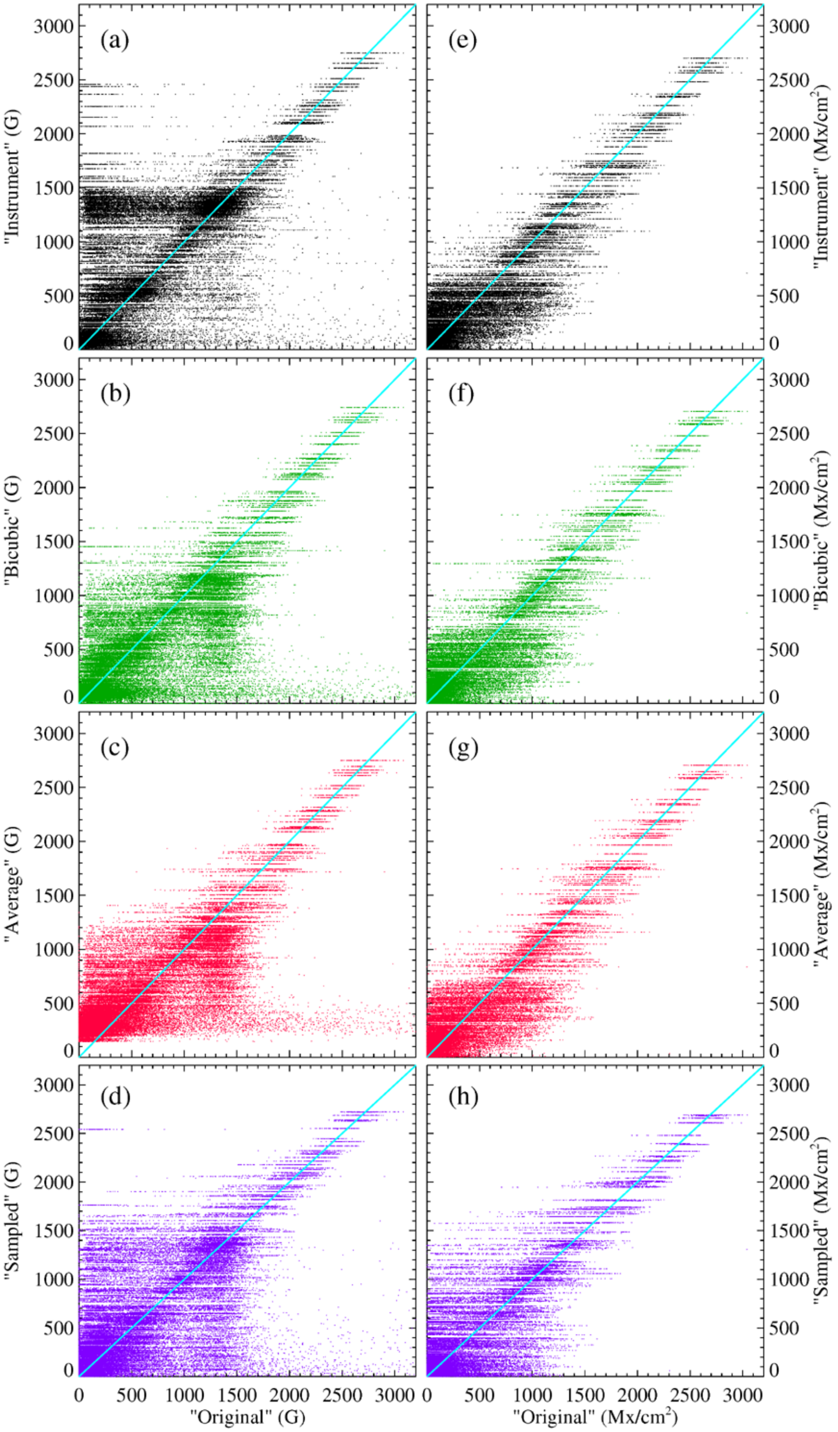

Figure 13 Follows Figure 4 for (a)–(d), except comparing the original *Hinode*/SP data with bin factor 16 results. Figures (e)–(h) follow the same format, but for the product $f \times B$.

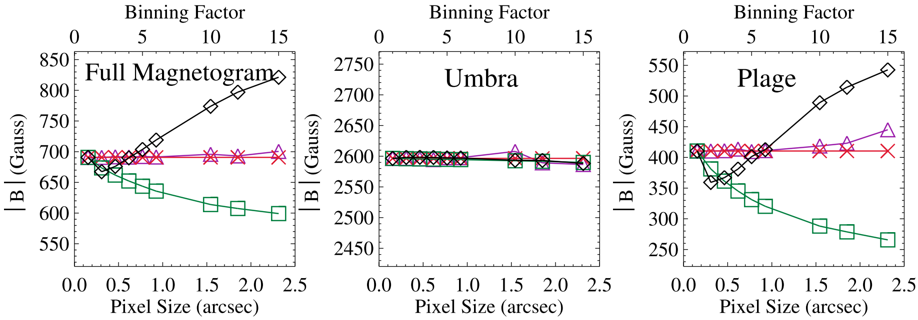

Figure 14 Following Figure 5, the average field strength over the target area, $\frac{1}{N}\sum B$ as a function of binning factor (top x-axis), for the four binning methods (**"instrument"** ◊, "bicubic" □, "average" × and "sampled" △), focusing on three areas as indicated: the full magnetogram, an "umbral" area and a "plage" area, as depicted in Figure 11. With the original *Hinode*/SP scan resolution of 0.15″, the resulting pixel sizes are also indicated (bottom x-axis).

Scatter plots of the inverted manipulated spectra demonstrate the general averaging which results with worsening spatial resolution (Figure 13). Of note in the *Hinode*/SP data, compared to the synthetic case (Figure 4), is the much greater spread in the original-resolution field strengths compared to the binned results. This behavior occurs primarily in "weak-field" or weak-polarization areas, where determining the field strength and fill fraction independently is arguably problematic; but that is not the case for all pixels. The product $f \times B$ is also shown; the distributions do change perceptibly (contrary to the synthetic case), with decreased scatter in weak-signal areas. (However, recall that only the "instrument" binning result is an independent inversion.) Primary contenders for the different behavior between B and $f \times B$ here, compared with the synthetic data, include the effects of photon noise and the contention that the original-resolution *Hinode*/SP data are unresolved to begin with.

Changes in the inferred magnetic field distribution in the observational data show similar trends with binning factor as was seen in the synthetic data. Beginning with field strength (Figure 14), the umbral area shows little change, but the plage area is quite sensitive to bin factor and to method used. The full field of view behaves closest to the plage.

The other inferred parameters examined here, the fill fraction, product $f \times B$, and instrument-frame inclination (Figure 15) confirm the general behavior observed in the synthetic-data experiments. The *Hinode*/SP data start with a wide range of inferred fill fraction present, and a median of less than 50% at full resolution for the full field of view (Figure 15). Again, the three post-facto binnings do an averaging or sampling, hence the mean of the fill fraction distribution stays the same although the range of values present decreases with bin factor. The "instrument" binning results in a decreasing mean and tighter range as the spatial resolution degrades, indicating that areas which were resolved become less so.

The product $f \times B$ shows a systematic decrease, on average, with worse spatial resolution – except from the "sampling" approach, which stays relatively constant. The "instrument" approach displays the most variation with resolution change, but the difference between it and the other methods is not as dramatic compared to the experiment with the model data.

The results for field inclination (Figure 15), show a distinct trend of the field becoming more aligned with the line of sight with decreasing spatial resolution, especially in the plage areas. In the umbra, there is effectively no change in the inclination angle distribution. The imperturbability of "sampling" against variations in inclination was seen earlier, as well;

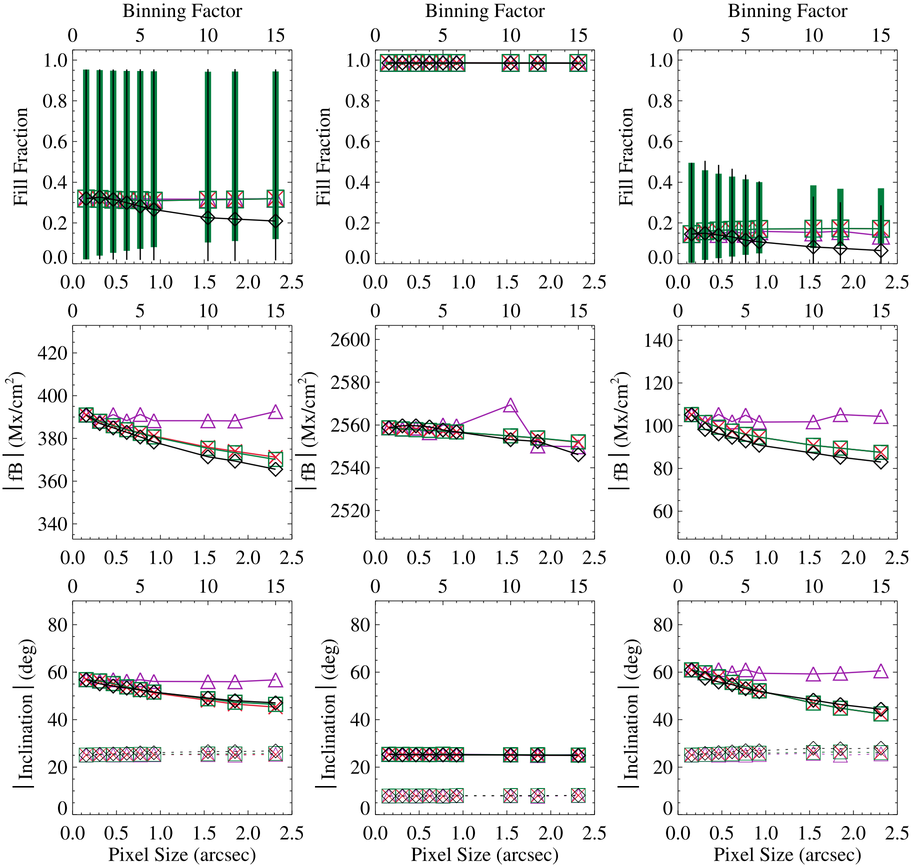

Figure 15 The same format as in Figure 14, Top row: Median (symbols) and 10th, 90th percentiles (displayed as "error bars") of inferred magnetic fill fraction as a function of bin factor. The three "post-facto" approaches consistently return the same fill fraction as the original observations, as expected. Middle row: The average product of the fill fraction and field strength, $\frac{1}{N}\sum fB$ as a function of binning factor. Bottom row: Variation of the average inclination angle with binning factor (thick line-connected curves), 0° indicates (unsigned) fields directed along the line of sight, or pure B_{los}, and 90° indicates field perpendicular to the line of sight or pure B_{trans} (here, $\gamma = \tan^{-1}(B_{\text{trans}}, |B_{\text{los}}|)$). Dot-connected curves indicate the standard deviation of the angle distribution.

again, the sampling should represent the underlying field distribution (until the super-pixels are themselves large and the resulting number of binned pixels available is small), since it samples rather than averages. We present the image-plane inclination angle from the line of sight – closely related to the direct observables, but related to the physical inclination of the field to the local normal by way of the observing angle. Since $\mu = 0.98$ for these data, the difference between image-plane and the heliographic-plane inclination from the local vertical direction is minimal.

The total unsigned magnetic flux, $\Phi = \sum f|B_z|dA$ behaves essentially the same in the umbral areas of both synthetic and *Hinode* data, varying little with resolution (except when there are arguably very few points within that area of interest, see Figure 16). And again, the full field-of-view behavior is dictated by what kind of structure dominates at highest resolution. We see that the "instrument" spectral binning and subsequent inversion, which

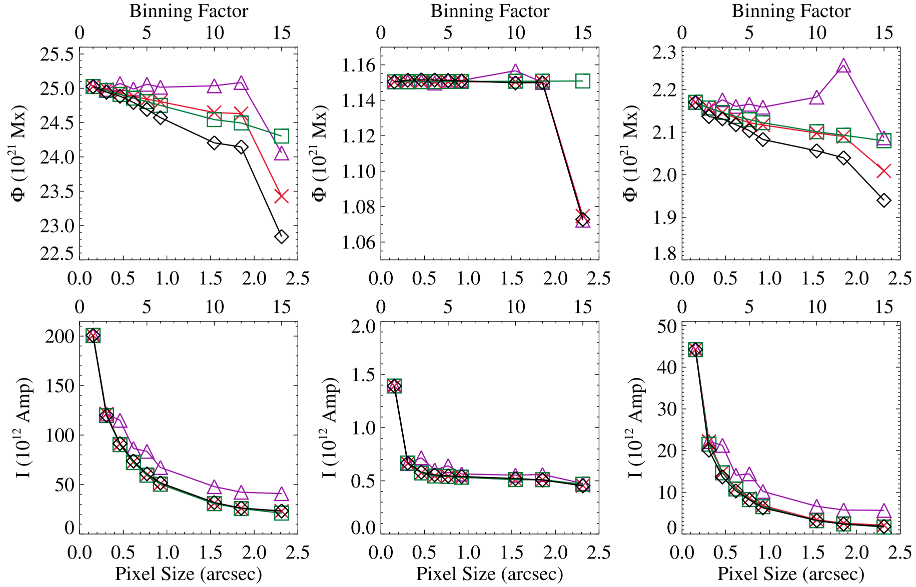

Figure 16 Comparison of parameters often used for characterizing active regions. Top: Variation of the total unsigned magnetic flux $\Phi = \sum f|B_Z|dA$ Bottom: Variation of the total unsigned electric current $I = \sum |J_Z|dA$. For these plots, the y-axis is allowed to vary.

is designed to mimic decreasing telescope size, produces more of an effect than the "post-facto" binning approaches.

The total vertical electric current is often used to parametrize an active region's stored magnetic energy (Leka and Barnes, 2003 and references therein). Could this characterization differ as a function of spatial resolution? In the *Hinode*/SP data, for all fields of view, there is a smooth decrease of total current with decreasing spatial resolution. In addition, all binning methods appear to act identically in this case. The behavior of the *Hinode*/SP data most resembles the synthetic "plage" beyond bin factor 10. That is, the observational data, even at $0.15''$, most closely resembles the area filled with unresolved multiple small-scale magnetic centers.

Overall, the plage area observed with *Hinode*/SP produces the most variations due to rebinning or degraded spatial resolution. The umbral area is least sensitive. The sampling typically provides the most consistent answer, but is also susceptible to the particular point sampled. The effect of changing the instrumental resolution more closely follows the results of the post-facto approaches as compared to the trends in the simulation data. Assuming that the behavior of the full magnetogram is characterized by the relative fraction of "resolved" or near-unity fill fraction pixels within the field of view, it is clear that the *Hinode*/SP data are dominated by non-unity fill fraction pixels and unresolved field structure, even at the highest resolution.

The Kolmogorov–Smirnoff tests confirm statistically what is described above. The cumulative probability curves for field strength (Figure 17), comparing the bin-10 results to the original resolution for both "instrument" and post-facto binnings indicate distinct differences in the full field of view which is reminiscent of the behavior in the plage area. The umbral field strength CPD looks almost identical to the umbral CPD for the synthetic data (Figure 8). The distribution of the vertical current density (Figure 17) shows an almost

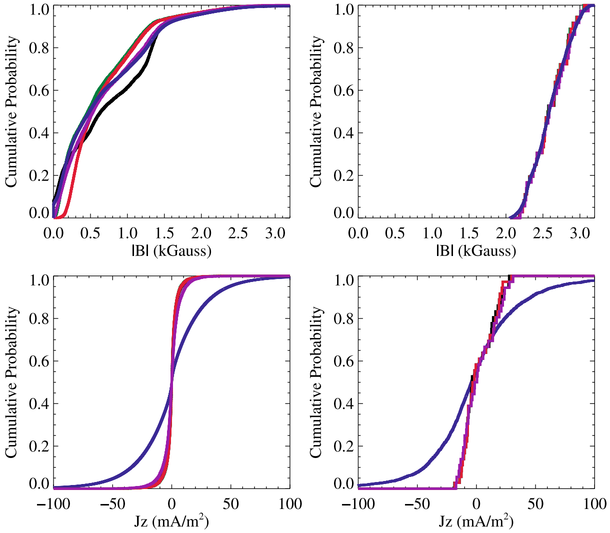

Figure 17 Cumulative probability distributions, for the full-resolution data and the bin-10 results, for the three fields of view (entirety, "umbra", and "plage" areas). For each, CPD curves are plotted for: original resolution, **instrument binning**, bicubic, average and sampled approaches. The top row is for the intrinsic field strength B, and the bottom row is for the vertical electric current density J_z.

exactly opposite behavior than was observed in the synthetic data, in that the original resolution indicates the presence of inferred vertical current which has decreased in magnitude significantly at bin factor 10.

The K–S statistics for field strength are more consistent across bin factors (Figure 18) than in the synthetic data: the D-statistic is slightly elevated but only varies dramatically with the simple binning. The K–S probability is unity for the plage area and the full field of view for all bin factors, indicating that the samples are not drawn from the same population. On the contrary, it can be argued that areas with consistent unity fill fraction statistically sample the same population as the underlying field.

On the other hand, the vertical current density is affected at all spatial resolutions (Figure 19). From a statistical point of view the results from lower resolution data do not represent the underlying distribution of the highest spatial resolution, even in the unity-fill-fraction umbral area. One may simply conclude that the actual distribution of vertical current in the solar photosphere is unknown and unknowable without absolutely full resolution everywhere in question.

5. Summary and Conclusions

We outline a manner by which to manipulate Stokes polarization spectra in order to mimic the effects of instrumental spatial resolution to the simplest order. Through the use of a synthetic magnetic field construct that is both fully resolved and contains small-scale structures, we apply this method to a range of degradations. We find (not surprisingly) that it is the highly structured areas which are most sensitive to the effects of instrumental optical spatial resolution.

The analysis indicates (also not surprisingly) that even the *Hinode*/SP "normal scan" spectro-polarimetric data at 0.15″ spatial sampling are unresolved. Recalling this, plus the

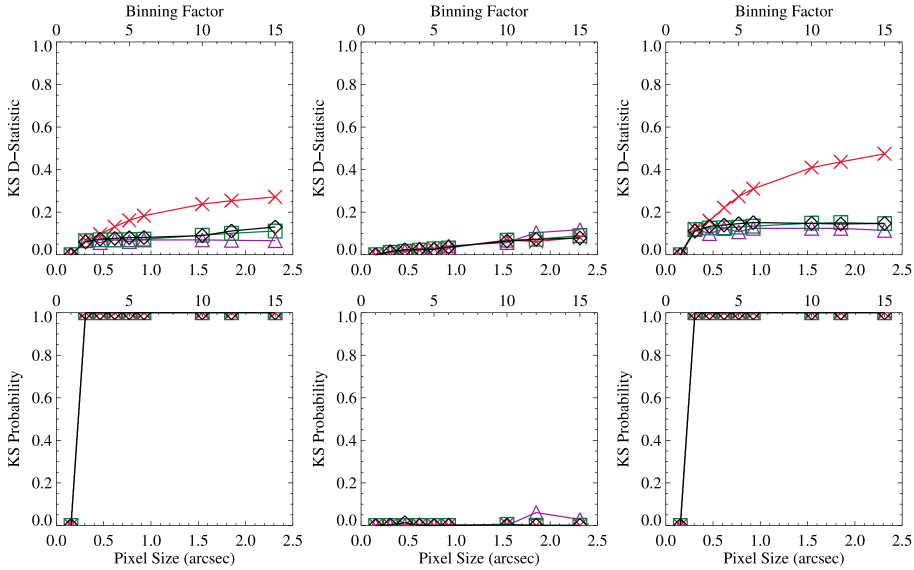

Figure 18 Summaries of the Kolmogorov–Smirnoff tests as a function of binning factor, for the intrinsic field strength B over the three fields of view. The top row shows the D-statistic, and the bottom row shows the probability P that the two samples are *different* (see text). Shown are curves for the original resolution *vs.* the (**"instrument"** $\Diamond$, "bicubic" $\Box$, "average" $\times$ and "sampled" $\triangle$) vertical current distributions.

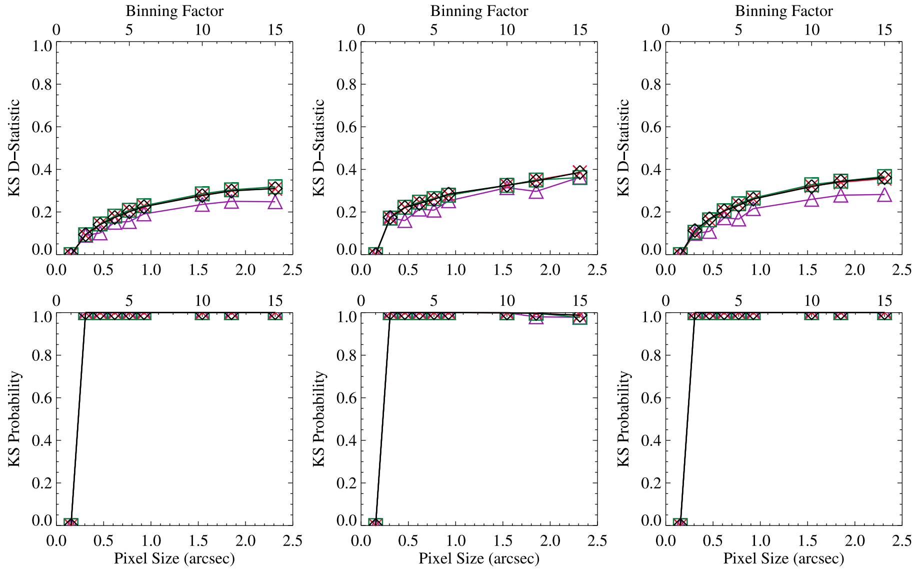

Figure 19 Summaries of the Kolmogorov–Smirnoff tests as a function of binning factor, for the vertical electric current density J_z, following Figure 18.

fact that we could only bin up to a factor of 16 before completely decimating the number of pixels needed for analysis, the patterns shown by field parameters with degrading resolution are remarkably similar to those found using the synthetic data. We thus confirm the appropriateness of the findings from these synthetic-data as valid for helping interpret the observational data.

Statistical tests confirm that whether by instrumental spectral mixing or post-facto methods, worsening spatial resolution results in a map of the vector field which does not reproduce the underlying magnetic structure, except in select areas where the returned magnetic filling factor in the binned data is still unity. Where the returned fill factor is less than unity, worsening spatial resolution leads to an average image-plane inclination angle more aligned to the line of sight, an increasing average field strength which couples with the decreasing average fill fraction to present a decreasing total magnetic flux. The behavior of further-derived parameters that rely on spatial derivatives is less straightforward, but may impart a non-zero current density and inferred "twist" where there in fact are none. The pessimistic interpretation of these results is that without the highest spatial resolution, the underlying field is unrecoverable. The optimistic interpretation is that by making use of the inferred magnetic fill fraction for inverted spectro-polarimetric data, it is possible to tell where these effects will be most dramatic, and where they will be least impactful.

The influence of spatial resolution on the instrument-plane inclination angle implies that the impacts on physically interpreted variables in the (coordinate-transformed) heliographic plane will vary with observing angle. This also has implications for our understanding of the large-scale "weak-field" areas from instruments of limited spatial resolution: in this context, the assumption that the photospheric field is dominantly radial (Wang and Sheeley, 1992; Arge *et al.*, 2002) must be re-examined.[7]

Details and caveats to the above statements are important to mention. There is no model of instrumental scattered light applied to (or subsequently corrected for) the synthetic data; in parallel, the *Hinode*/SP data are inverted using a common but simple treatment of computing a scattered light profile, rather than a more sophisticated local approach which has been demonstrated to better recover low-signal areas (Orozco Suárez *et al.*, 2007). While the details will differ had we used the latter, the approach taken here is consistent, and hence still illustrative. Effects as drastic as shown here are generated in the synthetic data without Doppler velocities or field gradients along the line of sight, whereas both are expected for observational data. Yet in the "simple is OK" defense, key behavior patterns are seen clearly in the *Hinode*/SP data.

We also ask how well instrumental resolution can be represented by "post-facto" manipulation of the vector-field map. Tests of three different methods show that, again, in highly structured underlying areas, these methods result in very different outcomes than expected from differences in aperture size. Simply put, there are only special cases where "binning down" a magnetogram will adequately mimic the differences between different instrumental spatial resolutions, and generally the "instrument" binning results in the largest differences from the underlying field.

This exercise of comparing the results when one simulates "worse spatial resolution" by different means is illuminating, and demonstrates that method matters according to the goal of the study in question. Three basic categories are: comparisons/calibrations between instruments, utilizing data from different instruments as part of an analysis for which data from a single instrument falls short (due to limited field of view, capability, availability, etc.), and interpreting numerical simulation results in the context of observations.

---

[7] As are the results that they may be predominantly horizontal, see Borrero and Kobel (2011).

Regarding the first category, we note that while a few instrument-comparison studies perform spatial averaging on the polarization signals for comparison (Wang *et al.*, 1992; Labonte, Mickey, and Leka, 1999),[8] the majority such studies published thus far use some form of "post-facto" averaging and binning applied to the magnetogram from the higher-resolution instrument (Berger and Lites, 2002, 2003; Tran *et al.*, 2005; Demidov *et al.*, 2008; Wang *et al.*, 2009a, 2009b). It is clear that "instrument" binning should be the preferred method, since all post-facto approaches result in a different (and typically smaller) variation with binning factor than expected from optical resolution.

An addendum to this category is using synthetic data for tests of algorithms through "hare & hound" exercises, where the evaluation depends crucially that the synthetic data mimic the behavior of those real data eventually slated for analysis. As such, including the gross effects of the instrument or observing method chosen (Leka *et al.*, 2009b; Orozco Suárez *et al.*, 2007) is needed in order to not arrive at incorrect conclusions.

In the second category, if the goal is to preserve the underlying character of the vector magnetic field *and* the region in question has a high average filling fraction, then post-facto binning can be employed with some confidence. However, as was shown with the vertical current density, while the magnetic field distribution and character may be preserved, quantities that are derived from the field must be viewed with less confidence. This is a very restrictive set of caveats, but the most well-defended position according to this study.

The third category acknowledges the great strides in simulations of solar magnetic structure, and the approach of validating them quantitatively using comparisons to observed structures (Leka and Steiner, 2001; Abbett, 2007; Orozco Suárez *et al.*, 2007; Sheminova, 2009). It is insufficient to rebin or apply a blurring function directly to a simulation's well-resolved output for comparisons to the solar observations. We reiterate that, due to these results, at the very least a simple modeling and manipulation of emergent spectra is required for even qualitative comparisons between simulations and observations of the magnetic field distribution.

In this context, we come back to Table 2 (see Appendix B, Table 4 and Figure 20). The minimal impact of the post-facto "congrid" approach on the *Hinode*/SP fast-scan map "Flux" $= \sum |B_{\mathrm{los}}|$ result is consistent with what we have shown here. The MDI Level 1.8.1 data used in Section 2 and in De Rosa *et al.* (2009) present a systematic offset from the Level 1.8.2 calibration (which became available December 2008, and decreased the B_{los} magnitudes by ≈ 8–9% in the location of AR 10953[9]). When variations in field of view, calibration, and especially spatial resolution are accounted for according to the findings of this paper (details can be found in Appendix B), there still exists an offset between the results from MDI and *Hinode*/SP that is larger than the quoted uncertainties, but may still be attributable to remaining differences in the lines' formation heights and inversion methods.

Finally, from this investigation, it is still unclear what the solar magnetic field structure actually *is*, especially for areas with fine-scale structure. This is not a new concept (Sánchez Almeida and Lites, 2000), but reinforced here through a simple, yet thorough demonstration. We show that our ignorance is especially true for quantities derived from the vector-field maps which rely on spatial derivatives (Parker, 1996; Leka *et al.*, 2009b). Are vector magnetic field maps useless? Definitely not! Comparisons between data of active regions obtained with consistent instrumentation and spatial resolution do detect differences amongst

---

[8] Labonte, Mickey, and Leka (1999) performed a near-simultaneous comparison between the IVM and the ASP, contrary to the note in Berger and Lites (2002), Section 1.1.

[9] See http://soi.stanford.edu/magnetic/Lev1.8/ for details.

the structures that must, somehow, be related to the inherent magnetic structure, especially as manifest in the release of stored magnetic energy (see, *e.g.*, Leka and Barnes, 2007 and references therein). But in the context of measuring and interpreting the state and behavior of the solar plasma, conclusions that are drawn must do so in the context of the limitations of the data employed.

Acknowledgements KDL first acknowledges Dr. Richard C. Canfield, who introduced her to spectropolarimetry and the interpretation of vector magnetic field maps (at $6''$ resolution!). We also appreciate the supportive and helpful comments from the referee. This work was made possible by the models and instruments developed under the following respective funding sources: NASA contracts NNH05CC75C, NNH09CE60C and NNH09CF22C, the NWRA subcontract from the Smithsonian Astrophysical Observatory under NASA NNM07AB07C, and the NWRA subcontract from Stanford University NASA Grant NAS5-02139 for SDO/HMI commissioning and pipeline code implementation. We thank Dr. Bruce Lites at NCAR/HAO for reformatter code and updates to the HAO inversion code. We also sincerely thank Mr. Eric Wagner for understanding "scientist code" and making things actually run. *Hinode* is a Japanese mission developed and launched by ISAS/JAXA, collaborating with NAOJ as a domestic partner, NASA and STFC (UK) as international partners. Scientific operation of the *Hinode* mission is conducted by the *Hinode* science team organized at ISAS/JAXA, consisting of scientists from institutes in the partner countries. Support for the post-launch operation is provided by JAXA and NAOJ (Japan), STFC (U.K.), NASA, ESA, and NSC (Norway). MDI data are provided by the SOHO/MDI consortium. SOHO is a project of international cooperation between ESA and NASA.

Appendix A: Constructing Representative Instrument-Binned Spectra When Only Demodulated Spectra Are Available

For an instrument like *Hinode*/SP, the demodulation from six states is performed on-board the spacecraft, so only the four demodulated states are available. Since the demodulated states do not contain all the information of the original states, we discuss here the impact of this loss of information on the noise level of the reconstructed states.

Assuming that each of the six polarization states actually observed at a given wavelength, $(I \pm P)(\lambda)$, is drawn from a Poisson distribution, the expectation value of each distribution is given by $\langle I \pm P\rangle \equiv p_{\pm}^{\lambda}$, where P can be any of Q, U or V. Since each of these is a Poisson distribution, the variance of each is equal to the expectation value.

The demodulated states actual available are given by

$$P(\lambda) \equiv \bigl[(I+P)(\lambda) - (I-P)(\lambda)\bigr]/2 \tag{1}$$

$$\begin{aligned} I(\lambda) \equiv \bigl[&(I+Q)(\lambda) + (I-Q)(\lambda) + (I+U)(\lambda) + (I-U)(\lambda) \\ &+ (I+V)(\lambda) + (I-V)(\lambda)\bigr]/6. \end{aligned} \tag{2}$$

(Henceforth, the wavelength dependence is assumed for clarity.) Working specifically with $I \pm Q$ as an example, since each modulated state will have similar behavior, the reconstructed modulated states are

$$\begin{aligned} (I \pm Q)_{\mathrm{R}} &= I \pm Q \\ &= \frac{1}{6}\bigl[(I+Q) + (I-Q) + (I+U) + (I-U) \\ &\quad + (I+V) + (I-V)\bigr] \pm \frac{1}{2}\bigl[(I+Q) - (I-Q)\bigr] \end{aligned}$$

$$
\begin{aligned}
&= \frac{2}{3}(I \pm Q) - \frac{1}{3}(I \mp Q) \\
&\quad + \frac{1}{6}\bigl[(I + U) + (I - U) + (I + V) + (I - V)\bigr]
\end{aligned}
\tag{3}
$$

which has an expectation value of

$$
\bigl\langle (I \pm Q)_{\mathrm{R}}(\lambda) \bigr\rangle = \frac{2q^{\lambda}_{\pm}}{3} - \frac{q^{\lambda}_{\mp}}{3} + \frac{u^{\lambda}_{+} + u^{\lambda}_{-} + v^{\lambda}_{+} + v^{\lambda}_{-}}{6},
\tag{4}
$$

and a variance of

$$
\operatorname{var}(I \pm Q)_{\mathrm{R}}(\lambda) = \frac{4q^{\lambda}_{\pm}}{9} + \frac{q^{\lambda}_{\mp}}{9} + \frac{u^{\lambda}_{+} + u^{\lambda}_{-} + v^{\lambda}_{+} + v^{\lambda}_{-}}{36},
\tag{5}
$$

whereas the expectation value and the variance of the actual state is simply $q^{\lambda}_{\pm}$. In the continuum (or anywhere the polarization is low), this reduces to

$$
\begin{aligned}
\operatorname{var}(I \pm Q)^{\mathrm{c}}_{\mathrm{R}} &= \frac{4q^{\mathrm{c}}_{\pm}}{9} + \frac{q^{\mathrm{c}}_{\mp}}{9} + \frac{u^{\mathrm{c}}_{+} + u^{\mathrm{c}}_{-} + v^{\mathrm{c}}_{+} + v^{\mathrm{c}}_{-}}{36} \\
&\approx \frac{2}{3} p^{\mathrm{c}}.
\end{aligned}
\tag{6}
$$

Thus the variance in the reconstructed modulated states, at least in areas of weak polarization, is smaller than the variance in the original states. Further, since each reconstructed state is the sum of six Poisson variables, rather than being a single Poisson variable (at a given wavelength), the distribution of the noise will also differ.

Appendix B: Comparing MDI and *Hinode*/SP Line-of-Sight "Flux"

As presented in this manuscript, instruments with different resolutions will provide quantitatively different descriptions of the solar magnetic field. We began the study with a provocative "why are these the same, and why are those different?" example. In detail, of course, there is more to this than simply the spatial resolution of two different instruments. The MDI data used for De Rosa *et al.* (2009) were from the level 1.8.1 calibration, the *Hinode*/SP data were provided by B.W. Lites, with ostensibly the same inversion that was used here for the "instrument"-binning exercise (although probably with slightly different implementation), but which also included a remapping to square pixels using an unknown method. Not only the spatial sampling but the field of view differs between the *Hinode*/SP scans of 18:35 and 22:30 UT, as one can see by closely examining Figures 1 and 11.

Here we demonstrate just how sensitive comparisons can be to the details of calibration, inversion, and very slight variations in the physical area sampled. Table 4 summarizes differences in the data sources and processing to obtain maps of AR 10953 on 30 April 2007, and Figure 20 shows the variation in the inferred $\Phi_{\mathrm{los}} = \sum |B_{\mathrm{los}}| dA$ for each. A full propagation of uncertainties was performed, for MDI following Hagenaar (2001), for *Hinode*/SP data using the uncertainties returned from inversions and propagated for B_{los}. For most points, the uncertainty is smaller than the plotting symbol.

The entries are combined into three rough groups. The first is based on the 18:35 UT *Hinode*/SP "normal" scan used for most of this paper, and the total $\sum |B_{\mathrm{los}}| dA$ based on it is deemed the reference. Entries include the results from post-facto "sampling" to match

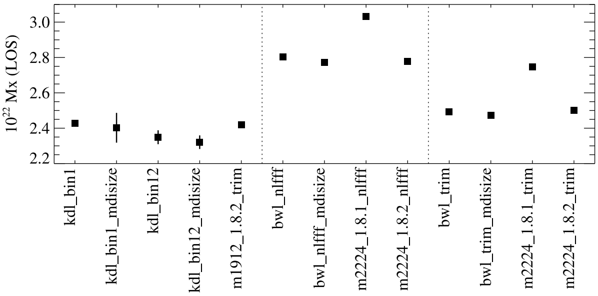

Figure 20 The total unsigned "flux" $\Phi_{\text{los}} = \sum |B_{\text{los}}| dA$ for NOAA AR 10953 on 30 April 2007 from various sources and methods of spatial resolution modeling. See Table 4 and text for descriptions of tags and the three groups indicated by vertical lines. Formal error bars are included for each point.

Table 4 AR 10953, 30 April 2007, Total $\sum |B_{\text{los}}| dA$ Details.

Label	Data source/Time	Details/Area	Difference (%)
kdl_bin1	*Hinode*/SP 18:35 "normal" scan	"instrument" bin-1	–
kdl_bin1_mdisize	" "	"kdl_bin1"+congrid → 1.98″	−1
kdl_bin12	" "	"instrument" bin-12	−3
kdl_bin12_mdisize	" "	"kdl_bin12"+congrid → 1.98″	−4
m1912_1.8.2_trim	MDI 19:12 UT[a] Level 1.8.2	[387:446,429:525][b]	−0.4
bwl_nlfff	*Hinode*/SP 22:30 "fast" map	Inversion by B.W. Lites for De Rosa *et al.* (2009). Remapped to square pixels	+15
bwl_nlfff_mdisize	" "	"bwl_nlfff"+congrid→ 1.98″	+14
m2224_1.8.1_nlfff	MDI 22:24 UT[c] Level 1.8.1	[385:460,429:509]	+25
m2224_1.8.2_nlfff	Level 1.8.2	" "	+14
bwl_trim	*Hinode*/SP 22:30 "fast" map	Trimmed in x-dir to match *Hinode*/SP 18:35	+3
bwl_trim_mdisize	" "	"bwl_trim"+congrid→ 1.98″	+2
m2224_1.8.1_trim	MDI 22:24 UT[c] Level 1.8.1	[400:461,428:509]	+13
m2224_1.8.2_trim	Level 1.8.2	" "	+3

[a] fd_M_96m_01d.5232.0012.fits.

[b] Indexing starts at 0.

[c] fd_M_96m_01d.5232.0014.fits.

the MDI resolution, and an "instrument" bin-12 to get close to the MDI resolution, with an additional sampling from that to match it exactly as indicated. These are compared to the MDI level 1.8.2 dataset closest in time.

The second and third groups are based on the 22:30 *Hinode*/SP "fast" scan (see Section 2), a post-facto "sampled" map based on it, and comparisons to the closest-time MDI level-1.8.1 and level-1.8.2 data. The difference between these two groups is whether the full 22:30 *Hinode*/SP is used or whether all are trimmed to match the (slightly) smaller field of view of the 18:35 UT *Hinode*/SP scan. The difference is not so slight.

Clearly, the binning approaches behave as described in the text, however those effects are insignificant as compared to even small discrepancies in the field of view and calibration. And evolution: comparing datasets which are as consistent as possible but separated by time, we see the active region increasing its total magnetic signal during this period (see Okamoto *et al.*, 2008).

The answer to the small puzzle presented in Section 2 is that in fact the level-1.8.1 MDI calibration produced systematically larger $\Phi_{\rm los}$ results than could otherwise be explained by spatial resolution issues; this is mostly accounted for by the recalibrated MDI level-1.8.2 data, as these examples show. And as we have demonstrated, post-facto manipulation of a magnetogram as in Section 2 does not generally reproduce the differences in instrumental spatial resolution. There exists still a small offset such that the level-1.8.2 data return a $\Phi_{\rm los} = \sum |B_{\rm los}| dA$ greater by a few percent than expected from the quoted uncertainties when the best possible match is compared (Table 4, "kdl_bin12" and "kdl_bin12_mdisize" vs. "m2224_1.8.2_trim"). We acknowledge that this is a single example, and invoke spectral-line properties and inversion method differences as probable contributors.

References

Abbett, W.P.: 2007, *Astrophys. J.* **665**, 1469. doi:10.1086/519788.

Arge, C.N., Hildner, E., Pizzo, V.J., Harvey, J.W.: 2002, *J. Geophys. Res.* **107**, 1319. doi:10.1029/2001JA000503.

Bao, S.D., Pevtsov, A.A., Wang, T.J., Zhang, H.Q.: 2000, *Solar Phys.* **195**, 75. doi:10.1023/A:1005244700895

Berger, T.E., Lites, B.W.: 2002, *Solar Phys.* **208**, 181. doi:10.1023/A:1020537923728

Berger, T.E., Lites, B.W.: 2003, *Solar Phys.* **213**, 213. doi:10.1023/A:1023953716633

Bommier, V., Landi Degl'Innocenti, E., Landolfi, M., Molodij, G.: 2007, *Astron. Astrophys.* **464**, 323. doi:10.1051/0004-6361:20054576.

Borrero, J.M., Kobel, P.: 2011, *Astron. Astrophys.* **527**, A29. doi:10.1051/0004-6361/201015634.

Canfield, R.C., de La Beaujardiere, J.-F., Fan, Y., Leka, K.D., McClymont, A.N., Metcalf, T.R., Mickey, D.L., Wuelser, J.-P., Lites, B.W.: 1993, *Astrophys. J.* **411**, 362. doi:10.1086/172836.

De Rosa, M.L., Schrijver, C.J., Barnes, G., Leka, K.D., Lites, B.W., Aschwanden, M.J., *et al.*: 2009, *Astrophys. J.* **696**, 1780. doi:10.1088/0004-637X/696/2/1780.

del Toro Iniesta, J.C., Orozco Suárez, D., Bellot Rubio, L.R.: 2010, *Astrophys. J.* **711**, 312. doi:10.1088/0004-637X/711/1/312.

Demidov, M.L., Balthasar, H.: 2009, *Solar Phys.* **260**, 261. doi:10.1007/s11207-009-9443-5.

Demidov, M.L., Golubeva, E.M., Balthasar, H., Staude, J., Grigoryev, V.M.: 2008, *Solar Phys.* **250**, 279. doi:10.1007/s11207-008-9225-5.

Grossmann-Doerth, U., Schüssler, M., Sigwarth, M., Steiner, O.: 2000, *Astron. Astrophys.* **357**, 351.

Hagenaar, H.J.: 2001, *Astrophys. J.* **555**, 448. doi:10.1086/321448.

Kosugi, T., Matsuzaki, K., Sakao, T., Shimizu, T., Sone, Y., Tachikawa, S., *et al.*: 2007, *Solar Phys.* **243**, 3. doi:10.1007/s11207-007-9014-6.

Labonte, B., Mickey, D.L., Leka, K.D.: 1999, *Solar Phys.* **189**, 1. doi:10.1023/A:1005202503425

Leka, K.D.: 1999, *Solar Phys.* **188**, 21. doi:10.1023/A:1005130630873

Leka, K.D., Barnes, G.: 2003, *Astrophys. J.* **595**, 1277. doi:10.1086/377511.

Leka, K.D., Barnes, G.: 2007, *Astrophys. J.* **656**, 1173. doi:10.1086/510282.

Leka, K.D., Steiner, O.: 2001, *Astrophys. J.* **552**, 354. doi:10.1086/320445.

Leka, K.D., Barnes, G., Crouch, A.: 2009a, In: Lites, B., Cheung, M., Magara, T., Mariska, J., Reeves, K. (eds.) *The Second Hinode Science Meeting: Beyond Discovery-Toward Understanding*, *ASP Conf. Ser.* **415**, 365.

Leka, K.D., Barnes, G., Crouch, A.D., Metcalf, T.R., Gary, G.A., Jing, J., Liu, Y.: 2009b, *Solar Phys.* **260**, 83. doi:10.1007/s11207-009-9440-8.

Lites, B.W., Skumanich, A.: 1990, *Astrophys. J.* **348**, 747. doi:10.1086/168284.

Lites, B.W., Elmore, D.F., Seagraves, P., Skumanich, A.P.: 1993, *Astrophys. J.* **418**, 928. doi:10.1086/173450.

Moon, Y., Kim, Y., Park, Y., Ichimoto, K., Sakurai, T., Chae, J., *et al.*: 2007, *Publ. Astron. Soc. Japan* **59**, 625.

Okamoto, T.J., Tsuneta, S., Lites, B.W., Kubo, M., Yokoyama, T., Berger, T.E., *et al.*: 2008, *Astrophys. J. Lett.* **673**, 215. doi:10.1086/528792.

Orozco Suárez, D., Bellot Rubio, L.R., Del Toro Iniesta, J.C., Tsuneta, S., Lites, B., Ichimoto, K., *et al.*: 2007, *Publ. Astron. Soc. Japan* **59**, 837.

Parker, E.N.: 1996, *Astrophys. J.* **471**, 485. doi:10.1086/177983.

Sanchez Almeida, J.: 1997, *Astrophys. J.* **491**, 993. doi:10.1086/304999.

Sánchez Almeida, J., Lites, B.W.: 2000, *Astrophys. J.* **532**, 1215. doi:10.1086/308603.

Sanchez Almeida, J., Landi Degl'Innocenti, E., Martinez Pillet, V., Lites, B.W.: 1996, *Astrophys. J.* **466**, 537. doi:10.1086/177530.

Scherrer, P.H., Bogart, R.S., Bush, R.I., Hoeksema, J.T., Kosovichev, A.G., Schou, J., *et al.*: 1995, *Solar Phys.* **162**, 129. doi:10.1007/BF00733429.

Sheminova, V.A.: 2009, *Solar Phys.* **254**, 29. doi:10.1007/s11207-008-9286-5.

Sigwarth, M., Balasubramaniam, K.S., Knölker, M., Schmidt, W.: 1999, *Astron. Astrophys.* **349**, 941.

Skumanich, A., Lites, B.W.: 1987, *Astrophys. J.* **322**, 473. doi:10.1086/165743.

Tran, T., Bertello, L., Ulrich, R.K., Evans, S.: 2005, *Astrophys. J. Suppl.* **156**, 295. doi:10.1086/426713.

Tsuneta, S., Ichimoto, K., Katsukawa, Y., Nagata, S., Otsubo, M., Shimizu, T., *et al.*: 2008, *Solar Phys.* **249**, 167. doi:10.1007/s11207-008-9174-z.

Ulrich, R.K., Evans, S., Boyden, J.E., Webster, L.: 2002, *Astrophys. J. Suppl.* **139**, 259. doi:10.1086/337948.

Ulrich, R.K., Bertello, L., Boyden, J.E., Webster, L.: 2009, *Solar Phys.* **255**, 53. doi:10.1007/s11207-008-9302-9.

Varsik, J.R.: 1995, *Solar Phys.* **161**, 207. doi:10.1007/BF00732067.

Wang, D., Zhang, M., Li, H., Zhang, H.: 2009a, *Sci. China G, Phys. Mech. Astron.* **52**, 1707. doi:10.1007/s11433-009-0249-0.

Wang, D., Zhang, M., Li, H., Zhang, H.Q.: 2009b, *Solar Phys.* **260**, 233. doi:10.1007/s11207-009-9441-7.

Wang, H., Varsik, J., Zirin, H., Canfield, R.C., Leka, K.D., Wang, J.: 1992, *Solar Phys.* **142**, 11. doi:10.1007/BF00156630.

Wang, Y., Sheeley, J.N.R.: 1992, *Astrophys. J.* **392**, 310. doi:10.1086/171430.

Zhang, H., Labonte, B., Li, J., Sakurai, T.: 2003, *Solar Phys.* **213**, 87. doi:10.1023/A:1023246421309